JGR Solid Earth

RESEARCH ARTICLE
10.1029/2022JB025286

Characteristics of the Matuyama-Brunhes Magnetic Field Reversal Based on a Global Data Compilation

Ahmed Nasser Mahgoub[1,2], **Monika Korte**[1], **and Sanja Panovska**[1]

[1]Helmholtz Centre Potsdam, Deutsches GeoForschungsZentrum GFZ, Section 2.3 – Geomagnetism, Potsdam, Germany, [2]Geology Department, Assiut University, Assiut, Egypt

Abstract Magnetic field reversals are irregular events in Earth's history when the geomagnetic field changes its polarity. Reversals are recorded by spot and continuous remanent magnetization data collected from lava flows and marine sediments, respectively. The latest field reversal, the Matuyama-Brunhes reversal (MBR), is better covered by paleomagnetic data than prior field reversals, hence providing an opportunity to understand the physical mechanisms. Despite the quantity of data, a full understanding of the MBR is still lacking. The evolution of the MBR in time and space is explored in this work by compiling a global set of paleomagnetic data, both from sediments and volcanic rocks, which encompass the period 900–700 ka. After careful evaluation of data and dating quality, regional and global stacks of virtual axial dipole moment (VADM), virtual geomagnetic pole (VGP), and paleosecular variation index (P_i) are constructed from the sediment records using bootstrap resampling. Individual VADMs and VGPs calculated from lavas are compared to these stacks. Four phases of full-vector field instability are observed in these stacks over the period 800–770 ka. The first three phases, observed at 800–785 ka, reflect a rapid weakening of the field coupled with low VGP latitude, after which the field returned to the reverse polarity of the Matuyama chron. The fourth phase, lasting from 780 to 770 ka, is when the field reversal process completed, such that the field entered the Brunhes normal polarity state. These findings point to a complex reversal process lasting ~30 Kyr, with the reversal ending at ~770 ka.

Plain Language Summary The Earth's magnetic field, or geomagnetic field, which humans and some animals use for navigation, shields us from solar and cosmic radiation. The magnetic North and South poles have repeatedly, but infrequently changed their positions over Earth's history, a phenomenon known as magnetic field reversal. During a reversal, the magnetic field intensity decreased to low levels, which could have had a detrimental impact on our planet as the magnetic shielding is diminished. The magnetic field last switched polarity from the Matuyama reverse state to the current Brunhes normal polarity in the most recent field reversal. This work used regional and global stacks of paleomagnetic sediment records with reasonable age control, to investigate the Matuyama-Brunhes reversal. From these stacks, we find that the last field reversal took ~30 Kyr to evolve, beginning at about 800 ka and ending at around 770 ka. Our data compilation indicates that the reversal lasted longer in records from high latitudes than low- to mid latitudes records, which confirms a previous suggestion that local reversal duration is latitudinal dependent.

Key Points:

- Global characteristics of the Matuyama-Brunhes field reversal were examined from well-dated high-quality lava and marine core data
- The Matuyama-Brunhes reversal started at 800 ka and the whole process lasted 30 ka
- The new data compilation generally confirms longer regional reversal duration at high latitudes compared to low latitudes

Supporting Information:

Supporting Information may be found in the online version of this article.

Correspondence to:

A. N. Mahgoub,
ahmedn@gfz-potsdam.de

Citation:

Mahgoub, A. N., Korte, M., & Panovska, S. (2023). Characteristics of the Matuyama-Brunhes magnetic field reversal based on a global data compilation. *Journal of Geophysical Research: Solid Earth*, *128*, e2022JB025286. https://doi.org/10.1029/2022JB025286

Received 12 AUG 2022
Accepted 7 JAN 2023

Author Contributions:

Conceptualization: Ahmed Nasser Mahgoub, Monika Korte, Sanja Panovska
Data curation: Ahmed Nasser Mahgoub, Sanja Panovska
Formal analysis: Ahmed Nasser Mahgoub
Funding acquisition: Ahmed Nasser Mahgoub
Investigation: Ahmed Nasser Mahgoub, Monika Korte, Sanja Panovska
Methodology: Ahmed Nasser Mahgoub, Monika Korte, Sanja Panovska
Project Administration: Ahmed Nasser Mahgoub, Monika Korte
Resources: Monika Korte

1. Introduction

The Matuyama-Brunhes reversal (MBR) is the most recent magnetic field reversal, and characterizing it globally is important to understand the geodynamo processes in Earth's core. Also, it is an essential chronozone boundary of the Quaternary magnetic polarity reversal timescale (Cande & Kent, 1995; Channell et al., 2020; Cohen & Gibbard, 2019; Ogg, 2020; Singer, 2014), therefore identifying its age is crucial for enhancing marine stratigraphy, correlation of rock sequences, and refining our understanding of global climate changes (Bassinot et al., 1994), among other applications. Marine and lacustrine sediments, lava flows, and ice cores are commonly used for MBR investigation. Despite the relative abundance of these data, different ages have been proposed for the MBR over the last decades: 730 ka (Imbrie et al., 1984; Mankinen & Dalrymple, 1979); 773 ka (Channell et al., 2010; Jouzel et al., 2007; Raisbeck et al., 2006; Singer et al., 2019; Valet et al., 2014); 780 ka (Shackleton et al., 1990); 783 ka (Mark et al., 2017); and 786 ka (Sagnotti et al., 2014, 2016), later revised to 783 or 780 (Sagnotti et al., 2019). However, the two most common ages proposed so far are 780 and 773 ka, and the latter was based on different archives, including lavas (Singer et al., 2019), marine sediments (Channell et al., 2020; Valet et al., 2014), and ice cores (Jouzel et al., 2007; Raisbeck et al., 2006). Integration of paleomagnetic data

Software: Ahmed Nasser Mahgoub, Monika Korte, Sanja Panovska
Supervision: Monika Korte
Validation: Ahmed Nasser Mahgoub, Monika Korte, Sanja Panovska
Visualization: Ahmed Nasser Mahgoub, Monika Korte, Sanja Panovska
Writing – original draft: Ahmed Nasser Mahgoub
Writing – review & editing: Ahmed Nasser Mahgoub, Monika Korte, Sanja Panovska

of these source materials, all with careful age assessment, lead Singer et al. (2019) to propose that the MBR occurred 773 Kyr ago. Distinct duration times were proposed for the MBR, which range from 1 to 10 Kyr (e.g., Clement, 2004; Singer et al., 2005) to ∼22 Kyr (Singer et al., 2019). A shorter duration, ≤1 Kyr, was also proposed from sediment cores located at Osaka Basin (Japan; Hyodo and Kitaba (2015)) and Lake Ohrid, Balkan (Just et al., 2019). Extremely quick sub-centennial duration for the polarity change were reported from directional changes in exceptionally high-resolution lacustrine deposits in Sulmona (Italy) (Sagnotti et al., 2014, 2016). The reliability of the isolated mean direction was questioned (Evans & Muxworthy, 2018). Sagnotti et al. (2019) re-sampled the section and confirmed that the MBR was properly documented. One interesting feature of the MBR duration is that it seems to increase with geographic latitude (Clement, 2004). We point out that the duration of the MBR is generally calculated from the field direction, by calculating the time when a record's virtual geomagnetic pole (VGP) latitude falls outside the stable polarity mean. However, it is well established that the strong directional changes during field reversals are associated with low field intensity levels (Singer et al., 2019; Van Zijl et al., 1962). As a result, it is more plausible to compute the duration taking both field directions and intensity into account.

The geometry of the MBR was investigated by tracking VGPs, known as VGP paths, calculated from lavas and sediment data of transitional polarity. Different assumptions were proposed from these paths, which include an axisymmetric transitional field (Clement & Kent, 1984; Hoffman & Fuller, 1978; Valet et al., 1988), longitudinally preferred VGP paths and VGP clusters (Clement, 1991; Laj, 1991; Valet et al., 1989), and a long-lived transitional field state (Hoffman, 2000). The validity of these assumptions were, however, questioned (Langereis et al., 1992; Prévot & Camps, 1993; Valet & Fournier, 2016). Also, Hartl and Tauxe (1996) have found a period of decrease in paleointensity ∼15 Kyr (at ∼795 ka) before the main MBR, known as precursor, from several sediment cores. This precursory event was found to be accompanied by significant directional change, from a series of volcanic records span from 180 to 0.78 Myr ago (Valet et al., 2012). The field precursor was also seen in records from the North Atlantic (Channell et al., 2004), North Pacific (Korff et al., 2016), Antarctica (Macrì et al., 2010), Mediterranean (Just et al., 2019; Sagnotti et al., 2014), and Indian Ocean (Valet et al., 2014). Following the polarity transition, Valet et al. (2012) observed another unstable geomagnetic phase with low-latitude VGPs, which they called a rebound. Unlike the precursor, the post-reversal rebound state was only documented in a few records (Singer et al., 2019). According to Valet et al. (2012), the durations of the precursory and rebound phases were estimated at 2.5 Kyr. The global magnetic field during MBR and its evolution in space and time were reconstructed using spherical harmonic (SH) models (Ingham & Turner, 2008; Leonhardt & Fabian, 2007; Shao et al., 1999). The iterative Bayesian inversion model of Leonhardt and Fabian (2007), called IMMAB4, indicates the existence of equatorial radial magnetic flux patches that move poleward during the MBR at the core-mantle boundary. Similarly, the Ingham and Turner (2008) SH model predicts low-latitude flux patches at ∼795 ka, which can be linked to the MBR precursor (Hartl & Tauxe, 1996). However, because the input data in these models are limited and may have certain issues with resolution and timescale reliability (see, e.g., Valet & Fournier, 2016), further global analyses on high quality data are required.

In order to precisely capture the field reversal behavior, lava samples should have precise age data (e.g., K-Ar and $^{40}Ar/^{39}Ar$) with uncertainty values lower than duration of the field reversal itself. Also, well-dated sediment cores with high sedimentation rate (SR) and temporal resolution better than the reversal duration are needed. Ideally, the age uncertainty of lavas should not exceed few hundreds of years, and the temporal resolution of sediments should be lower than this limit to properly define the reversal. For sediments, in order to have a record with 200 year resolution, the SR should be greater than 10 cm/Kyr (Roberts & Winklhofer, 2004), but some additional factors, such as presumption of constant and continuous SR and type of sample discrete or U-channels, (e.g., Roberts, 2006; Sagnotti et al., 2016) are fundamental as well. A second issue is the ability of a paleomagnetic sample to reliably retain paleomagnetic field components (declination, inclination, and intensity) during the reversal when field intensity reaches minimal values (Singer et al., 2019). In this context, lava samples are preferable because they acquire the paleomagnetic field information by thermal remanent magnetization (TRM), for which the theoretical background is well established (see Néel, 1955). Sediment-derived detrital, depositional, and post-depositional remanent magnetization (PDRM), on the other hand, has some limitations in terms of, among others, signal smoothing (Lund & Keigwin, 1994), potential inclination shallowing (Arason & Levi, 1990; Deamer & Kodama, 1990), and lock-in depth (Channell et al., 2004; Lund & Keigwin, 1994; Sagnotti et al., 2005), which can significantly impair their dependability. Moreover, the magnetization acquisition processes in sediments decrease their efficiency in recording the field during transitions (Valet & Fournier, 2016).

However, (P)DRM data are continuous while lavas only give scattered TRM data, therefore sediment cores are more efficient for investigating the temporal evolution of the field reversal. The best solution is an integration of different inputs, as done by Singer et al. (2019).

In this study, we evaluate the MBR by combining the time series of 38 sediment cores with independent age models, selected from a total of 68 records distributed over 16 regions of the globe. Half of these cores have mid-to high SR in the range of 5–16 cm/Kyr, so we expect to have a reasonable resolution. The data, their selection and treatment are described in Section 2, including regional consistency checks. Some global characteristics of the magnetic field during the MBR are inferred from regional and global stacks of VGP and virtual axial dipole moments (VADM) of these data in Section 3. Volcanic data are included in this analysis. We estimate the time and duration of the last field reversal, using a global stack of the paleosecular variation index (Panovska & Constable, 2017) in Section 4. The relation between duration and local site latitude is also discussed there.

2. Data Compilation and Treatment

Paleomagnetic data from lavas and marine cores have been compiled and analyzed in this study. We included all data, accessible to us, of the age period 900–700 ka. The compilation process was completed by carefully assessing the original articles, and by using open-access global databases, such as the Absolute Paleointensity database (PINT; Bono et al., 2022); PANGAEA (https://www.pangaea.de/) and Magnetics Information Consortium (MagIC; https://www2.earthref.org/MagIC). Also, we consider the compilations SEDPI06 (Tauxe & Yamazaki, 2007, 2015) and PADM2M (Ziegler et al., 2011), where the relative paleointensity (RPI) data of sediment records were provided.

The next sections summarize how we compiled and examined age and paleomagnetic data of lavas and sediments records. More details about the compilation and evaluations processes are available in the Texts S1 and S2 in Supporting Information S1, respectively.

2.1. Lava Data

We compiled paleomagnetic data from lavas with only absolute radioisotope, $^{40}Ar/^{39}Ar$ and K-Ar, age data. Lavas that have been dated relatively using magnetic polarity and stratigraphy are not included in this study. Considering this dating constraint, a number of 108 lava sites have been compiled, and 107 site-mean directions and 42 site-mean absolute paleointensities (PI) were calculated from them. Table 1 contains a list of these sites in terms of geographic location, ages, paleomagnetic directions, and PIs. The distribution of compiled lavas is illustrated in Figure 1a, which reveals that lavas were reported from 11 regions (Tahiti, Hawaii, Guadalupe, Chile, Canary Islands, Azores Islands, Iceland, NW-USA, Mexico, Germany, and Antarctica). Six of the 11 lava regions are located in the western hemisphere, three are located along the Atlantic (longitude ~335–343°E), and only two are located in the eastern hemisphere. Of the 108 sites, 29 have K-Ar ages while the rest were $^{40}Ar/^{39}Ar$ dated.

Our compilation is based on the latest version of the PINT database (http://www.pintdb.org/), which contains 200 PI data points for the period 700–900 ka, 198 of them from lava flows. In terms of age, these 198 data points were dated as follows: 91 have $^{40}Ar/^{39}Ar$ ages, 26 with K-Ar, and the remainder have been dated by relative means (magnetic polarity and stratigraphy). By considering only absolute ages, only 117 lava sites remain. We found that certain sites in PINT include absolute $^{40}Ar/^{39}Ar$ age data, but the original papers where these data were cited had no such absolute ages. For instance, we compiled 10 $^{40}Ar/^{39}Ar$ dated lava sites from Chile, whereas PINT reported 15 sites. After examining them, we noticed that the five extra sites in PINT had not been assigned $^{40}Ar/^{39}Ar$ age data. Moreover, we consider data updates; when a lava flow is re-sampled for new age estimates or PI measurements, we include only the most recent updates if their quality is superior. An example for that is PI data reported from La Guadeloupe Island. Carlut et al. (2000) obtained PI data from three La Guadeloupe Island lava sites, which were then resampled for new $^{40}Ar/^{39}Ar$ age estimations (M. C. Brown et al., 2013) and PI measurements (M. C. Brown et al., 2009). We take these updates into account in terms of ages (M. C. Brown et al., 2013) and average the PI data of the two studies (M. C. Brown et al., 2009; Carlut et al., 2000). Also, we note that some of the PI data from previous works were rejected by us since further analysis revealed that their ages were not in logical sequence with their stratigraphic context; see Text S1 and Figure S1 in Supporting Information S1 for more information. This explains why the PINT data set is larger than our final data set.

It is known that conventional K-Ar ages are not as accurate as $^{40}Ar/^{39}Ar$, because insufficient degassing of sanidine crystals can result in too young results (McDowell, 1983; Sarna-Wojcicki et al., 2000; Webb &

Journal of Geophysical Research: Solid Earth

10.1029/2022JB025286

Table 1
Summary of 108 Sites Compiled From Eleven Volcanic Regions

Site	Age (ka)	Error (ka)	Dating-method	Recal. age (ka)	VGP lat (°N)	A_{95} (°)	VADM (10^{22}–Am^2)	S.D. (10^{22}–Am^2)	Q_{PI}	Reference (age)	Reference (paleomagnetic direction)	Reference (PI)
(1) Tahiti (−17.8°N/210.3°E)												
B5	772.6	9.3	$^{40}Ar/^{39}Ar$	771.8	74.6	3.1	3.1	0.3	4	Singer et al. (2019)	Mochizuki et al. (2011)	Mochizuki et al. (2011)
B4	781.3	3.9	$^{40}Ar/^{39}Ar$	781.3	75.4	3.0	4.8	na	4	Balbas et al. (2018)	Mochizuki et al. (2011)	Mochizuki et al. (2011)
B3	774.4	8.7	$^{40}Ar/^{39}Ar$	773.6	81.5	2.0	4.0	1.1	4	Singer et al. (2019)	Mochizuki et al. (2011)	Mochizuki et al. (2011)
B2	791.1	4.6	$^{40}Ar/^{39}Ar$	790.2	62.5	11.8				Singer et al. (2019)	Mochizuki et al. (2011)	
A28	792.4	3.8	$^{40}Ar/^{39}Ar$	791.5	−24.5	9.0				Singer et al. (2019)	Mochizuki et al. (2011)	
B1	795.5	6.7	$^{40}Ar/^{39}Ar$	794.6	−71.9	19.9				Singer et al. (2019)	Mochizuki et al. (2011)	
A27	795.1	4.0	$^{40}Ar/^{39}Ar$	795.1	−63.8	8.6				Singer et al. (2019)	Balbas et al. (2018)	
A24	801.1	6.7	$^{40}Ar/^{39}Ar$	800.2	43.5	13.0				Singer et al. (2019)	Mochizuki et al. (2011)	
A23	800.9	3.6	$^{40}Ar/^{39}Ar$	800.9	63.0	16.1				Balbas et al. (2018)	Mochizuki et al. (2011)	
A22	793.6	4.6	$^{40}Ar/^{39}Ar$	792.7	61.3	9.9				Singer et al. (2019)	Mochizuki et al. (2011)	
A29	805.1	4.6	$^{40}Ar/^{39}Ar$	805.1	66.9	6.3				Balbas et al. (2018)	Mochizuki et al. (2011)	
A17	794.4	6.7	$^{40}Ar/^{39}Ar$	793.5	−56.5	10.0	0.6	0.5	3	Singer et al. (2019)	Mochizuki et al. (2011)	Mochizuki et al. (2011)
A16	819	13.0	$^{40}Ar/^{39}Ar$	818.1	−70.0	10.3				Singer et al. (2019)	Mochizuki et al. (2011)	
TT	777.4	6.1	$^{40}Ar/^{39}Ar$	776.5	−34.0	1.6				Singer et al. (2019)	Chauvin et al. (1990)	
RIV	774.4	5.4	$^{40}Ar/^{39}Ar$	773.6	−33.1	8.5				Singer et al. (2019)	Chauvin et al. (1990)	
RIT	777	6.9	$^{40}Ar/^{39}Ar$	776.1	−41.9	3.3				Singer et al. (2019)	Chauvin et al. (1990)	
RIS	789.1	6.2	$^{40}Ar/^{39}Ar$	788.2	−73.5	7.8				Singer et al. (2019)	Chauvin et al. (1990)	
RID	879	6	$^{40}Ar/^{39}Ar$	879	−52.7	4.1				Singer et al. (2019)	Chauvin et al. (1990)	
(2) Hawaii (20.8°N/203.7°E)												
61	725.6	5.2	$^{40}Ar/^{39}Ar$	724.8	84.2	2.2	6.2	0.2	3	Singer et al. (2019)	Coe et al. (2004)	Singer et al. (2019)
60	749.2	3.5	$^{40}Ar/^{39}Ar$	748.4	86.5	4.3	5.5	0.1	3	Singer et al. (2019)	Coe et al. (2004)	Singer et al. (2019)
59	771	4.5	$^{40}Ar/^{39}Ar$	770.2	−44.2	6.9	2.4	0.1	3	Singer et al. (2019)	Coe et al. (2004)	Singer et al. (2019)
58	770.8	4.2	$^{40}Ar/^{39}Ar$	770.0	−47.9	2.8	1	na	3	Singer et al. (2019)	Coe et al. (2004)	Singer et al. (2019)
52	773.9	3.5	$^{40}Ar/^{39}Ar$	773.1	−38.2	2.6				Singer et al. (2019)	Coe et al. (2004)	
51	775.7	4.3	$^{40}Ar/^{39}Ar$	774.8	−16.7	10.2				Singer et al. (2019)	Coe et al. (2004)	
44	773.4	6.3	$^{40}Ar/^{39}Ar$	772.6	62.0	4.5				Singer et al. (2019)	Coe et al. (2004)	
37	771.7	3.6	$^{40}Ar/^{39}Ar$	770.9	−67.5	3.5	0.6	na	3	Singer et al. (2019)	Coe et al. (2004)	Singer et al. (2019)
35	864.0	7.0	$^{40}Ar/^{39}Ar$	864.0	−26.4	5.3	1.6	na	3	Singer et al. (2019)	Coe et al. (2004)	Singer et al. (2019)
34	871.0	15.0	$^{40}Ar/^{39}Ar$	871.0	−20.3	3.3				Singer et al. (2019)	Coe et al. (2004)	
21	863.0	8.0	$^{40}Ar/^{39}Ar$	863.0	−18.9	4.7				Singer et al. (2019)	Coe et al. (2004)	
6	787.0	12.0	$^{40}Ar/^{39}Ar$	794.1	−51.6	na				Baksi et al. (1992)	Baksi et al. (1992)	
5	780.0	10.0	$^{40}Ar/^{39}Ar$	787.1	27.6	na				Baksi et al. (1992)	Baksi et al. (1992)	
4	772.0	14.0	$^{40}Ar/^{39}Ar$	779.0	−50.7	na				Baksi et al. (1992)	Baksi et al. (1992)	

Journal of Geophysical Research: Solid Earth
10.1029/2022JB025286

Table 1
Continued

Site	Age (ka)	Error (ka)	Dating-method	Recal. age (ka)	VGP lat (°N)	A_{95} (°)	VADM (10^{22}–Am^2)	S.D. (10^{22}–Am^2)	Q_{PI}	Reference (age)	Reference (paleomagnetic direction)	Reference (PI)
M/PGB-6+PGA-7	701.0	29.0	$^{40}Ar/^{39}Ar$	716.1	76.8	3.5				Leonhardt et al. (2009)	Leonhardt et al. (2009)	
(3) Guadeloupe (16.1°N/298.3°E)												
GU22	746.0	13.0	K-$Ar^{(CG)}$	na	86.1	1.6				Carlut et al. (2000)	Carlut et al. (2000)	
GU13	784.0	19.0	K-$Ar^{(CG)}$	na	86.5	2.5	6.7	1.1	1	Blanc (1983)	Carlut et al. (2000)	Quidelleur and Valet (1996)
G03	783.0	31.0	K-$Ar^{(CG)}$	na	83.1	3.0	3.8	1.2	4*	Carlut et al. (2000)	M. C. Brown et al. (2009)	Quidelleur and Valet (1996)
G02	786.0	15.0	$^{40}Ar/^{39}Ar$	785.1	−61.0	13.0	1.7	1.0	3*	Singer et al. (2019)	M. C. Brown et al. (2009) M. C. Brown et al. (2009)	Quidelleur and Valet (1996)
G01	786.3	7.5	$^{40}Ar/^{39}Ar$	785.4	−14.4	12.4	1.3	0.4	3*	Singer et al. (2019)	M. C. Brown et al. (2009)	M. C. Brown et al. (2009)
GD01	783.5	6.8	$^{40}Ar/^{39}Ar$	782.6	−79.0	7.4	5.1	1.0	3*	Singer et al. (2019)	M. C. Brown et al. (2009)	M. C. Brown et al. (2009)
GU49	770.0	50.0	K-$Ar^{(CG)}$	na	71.4	9.1				Samper et al. (2007) Ricci et al. (2017)	Ricci et al. (2018)	–
GU43	759.0	14.0	K-$Ar^{(CG)}$	na	79.9	5.4				Samper et al. (2007) Ricci et al. (2017)	Ricci et al. (2018)	
GU42	777.0	15.0	K-$Ar^{(CG)}$	na	62.1	5.2				Ricci et al. (2018)	Ricci et al. (2018)	
GU40	791.0	12.0	K-$Ar^{(CG)}$	na	−84.6	3.3				Samper et al. (2007) Ricci et al. (2017)	Ricci et al. (2018)	
(4) Chile (−36.0°N/289.0°E)												
QTW10-10	782	5.1	$^{40}Ar/^{39}Ar$	781.10	−25.6	8.8	0.9	0.0	4	Singer et al. (2019)	L. L. Brown et al. (2004)	Gratton et al. (2007)
QTW10-05	784.2	3.1	$^{40}Ar/^{39}Ar$	783.30	−18.6	8.4				Singer et al. (2019)	L. L. Brown et al. (2004)	
QTW10-03	785.3	3.8	$^{40}Ar/^{39}Ar$	784.40	−8.9	11.7	2.7	0.4	2	Singer et al. (2019)	L. L. Brown et al. (2004)	Gratton et al. (2007)
QTW10-02	811.0	30.0	$^{40}Ar/^{39}Ar$	816.0	−72.9	7.3	1.6	0.1	3	L. L. Brown et al. (2004)	L. L. Brown et al. (2004)	Gratton et al. (2007)
QTW11-20	740.4	7.2	$^{40}Ar/^{39}Ar$	739.6	87.4	2.8	8.4	0.2	4*	Singer et al. (2019)	L. L. Brown et al. (2004)	Gratton et al. (2007)
QTW11-19	758	21.0	$^{40}Ar/^{39}Ar$	757.2	80.2	2.9				Singer et al. (2019)	L. L. Brown et al. (2004)	
QTW11-16	781.7	5.8	$^{40}Ar/^{39}Ar$	780.8	−24.8	3.6				Singer et al. (2019)	L. L. Brown et al. (2004)	
QTW11-11	781.4	5.6	$^{40}Ar/^{39}Ar$	780.50	−26.1	3.3				Singer et al. (2019)	L. L. Brown et al. (2004)	
QTW11-05	786.3	5.3	$^{40}Ar/^{39}Ar$	785.4	−25.7	3.6	1.1	0.2		Singer et al. (2019)	L. L. Brown et al. (2004)	Gratton et al. (2007)
QTW11-03	785	6.6	$^{40}Ar/^{39}Ar$	784.1	−21.8	5.9				Singer et al. (2019)	L. L. Brown et al. (2004)	
(5) Canary islands (28.8°N/342.2°E)												
LL101	780.0	90.0	K-$Ar^{(conv)}$	na	84.2	5.7				Abdel-Monem et al. (1972)	Quidelleur and Valet (1996)	
LS116	797.0	12.0	K-$Ar^{(CG)}$	na	−58.0	10.9				Quidelleur et al. (2002)	Quidelleur and Valet (1996)	
LS118	821.0	13.0	K-$Ar^{(CG)}$	na	−51.0	2.5	1.5	0.2	2	Quidelleur et al. (2002)	Quidelleur and Valet (1996)	Quidelleur and Valet (1996)

Journal of Geophysical Research: Solid Earth
10.1029/2022JB025286

Table 1
Continued

Site	Age (ka)	Error (ka)	Dating-method	Recal. age (ka)	VGP lat (°N)	A_{95} (°)	VADM (10^{22}–Am^2)	S.D. (10^{22}–Am^2)	Q_{PI}	Reference (age)	Reference (paleomagnetic direction)	Reference (PI)
LS119	825.0	15.0	K-Ar$^{(CG)}$	na	−74.0	4.4	6.6	0.8	2	Quidelleur et al. (2002)	Quidelleur and Valet (1996)	Quidelleur and Valet (1996)
ME47	788.0	12.0	K-Ar$^{(CG)}$	na	71.9	2.3	7.1	0.7	3	Quidelleur et al. (2003)	Valet et al. (1999)	M. C. Brown et al. (2009)
ME45	784	13.0	K-Ar$^{(CG)}$	na	−61.4	1.4	1.5	na	3	Quidelleur et al. (2003)	Valet et al. (1999)	Valet et al. (1999)
ET18	705	12.0	K-Ar$^{(CG)}$	na	68.6	3.7	7.1	0.6	3	Valet et al. (1999)	Valet et al. (1999)	Valet et al. (1999)
ET06	751	13.0	K-Ar$^{(CG)}$	na	67.6	2.6	7.7	1.0	3	Valet et al. (1999)	Valet et al. (1999)	Valet et al. (1999)
TS12	751.9	18.1	^{40}Ar/^{39}Ar	746.3	74.8	5.5				Singer et al. (2002)	Singer et al. (2002)	
TN16	771.7	4.3	^{40}Ar/^{39}Ar	770.9	−5.4	43.5				Singer et al. (2019)	Singer et al. (2002)	
TN17	774.3	7.9	^{40}Ar/^{39}Ar	773.5	−31.1	5.3				Singer et al. (2019)	Singer et al. (2002)	
TN20	774.8	5.3	^{40}Ar/^{39}Ar	774.0	−31.6	8.7				Singer et al. (2019)	Singer et al. (2002)	
TS16	849.8	45.1	^{40}Ar/^{39}Ar	842.7	−77.2	3.0				Singer et al. (2002)	Singer et al. (2002)	
BN6	786.0	12.0	K-Ar$^{(CG)}$	na	63.2	3.6				Quidelleur et al. (2003)	Quidelleur et al. (2003)	
BS4	790.0	12.0	K-Ar$^{(CG)}$	na	50	4.1				Quidelleur et al. (2003)	Quidelleur et al. (2003)	
MO8	718.0	11.0	K-Ar$^{(CG)}$	na	50	4.1				Quidelleur et al. (2003)	Quidelleur et al. (2003)	
BN4	782.0	12.0	K-Ar$^{(CG)}$	na	−83.4	2.8				Quidelleur et al. (2003)	Quidelleur et al. (2003)	
BS2	795.0	12.0	K-Ar$^{(CG)}$	na	−79.1	3.6				Quidelleur et al. (2003)	Quidelleur et al. (2003)	
(6) Azores islands (37.8°N/334.9°E)												
AZ27	776.0	12.0	^{40}Ar/^{39}Ar	792.7	−74.2	1.7				Johnson et al. (1998)	Johnson et al. (1998)	
AZ23	785.0	11.0	^{40}Ar/^{39}Ar	801.9	−75.8	1.7				Johnson et al. (1998)	Johnson et al. (1998)	
AZ17	819.0	17.0	^{40}Ar/^{39}Ar	836.6	−78.1	3.7				Johnson et al. (1998)	Johnson et al. (1998)	
AZ13	835.0	11.0	^{40}Ar/^{39}Ar	852.9	−68.8	2.0				Johnson et al. (1998)	Johnson et al. (1998)	
AZ26	793.0	8.0	^{40}Ar/^{39}Ar	810	−69.7	6.5				Johnson et al. (1998)	Johnson et al. (1998)	
AZ25	814.0	17.0	^{40}Ar/^{39}Ar	831.5	−76.1	3.9				Johnson et al. (1998)	Johnson et al. (1998)	
AZ24	817.0	14.0	^{40}Ar/^{39}Ar	834.5	−74.7	1.8				Johnson et al. (1998)	Johnson et al. (1998)	
AZ18	849.0	14.0	^{40}Ar/^{39}Ar	867.2	−76.8	2.3				Johnson et al. (1998)	Johnson et al. (1998)	
AZ14	846.0	11.0	^{40}Ar/^{39}Ar	864.2	−45.2	1.9				Johnson et al. (1998)	Johnson et al. (1998)	
AZ19	852.0	10.0	^{40}Ar/^{39}Ar	870.3	−75.4	2.2				Johnson et al. (1998)	Johnson et al. (1998)	
AZ16	843.0	9.0	^{40}Ar/^{39}Ar	861.1	−70.8	4.5				Johnson et al. (1998)	Johnson et al. (1998)	
SM50	763.0	11.0	K-Ar$^{(CG)}$	na	53.5	2.8	1.4[a]	na	1**	Ricci et al. (2020)	Ricci et al. (2020)	Ricci et al. (2020)
SM23	765.0	5.0	K-Ar$^{(CG)}$	na	37.5	4.5	0.9[a]	na	1**	Ricci et al. (2020)	Ricci et al. (2020)	Ricci et al. (2020)
SM15	762.0	11.0	K-Ar$^{(CG)}$	na	73.3	5.3	4.6[a]	na	1**	Ricci et al. (2020)	Ricci et al. (2020)	Ricci et al. (2020)
SM12	768.0	5.0	K-Ar$^{(CG)}$	na	30.2	5.8	0.3[a]	na	1**	Ricci et al. (2020)	Ricci et al. (2020)	Ricci et al. (2020)
SM18	789.0	11.0	K-Ar$^{(CG)}$	na	−70.5	5.9	6.4[a]	na	1**	Ricci et al. (2020)	Ricci et al. (2020)	Ricci et al. (2020)

Journal of Geophysical Research: Solid Earth

10.1029/2022JB025286

Table 1
Continued

Site	Age (ka)	Error (ka)	Dating-method	Recal. age (ka)	VGP lat (°N)	A_{95} (°)	VADM (10^{22}–Am^2)	S.D. (10^{22}–Am^2)	Q_{PI}	Reference (age)	Reference (paleomagnetic direction)	Reference (PI)
(7) Iceland (66.1°N/342.8°E)												
GS9	768.0	53.0	^{40}Ar/^{39}Ar	762.3	85.4	18.0				Camps et al. (2011)	Camps et al. (2011)	
GS8	809.0	73.0	^{40}Ar/^{39}Ar	803	81.2	13.5				Camps et al. (2011)	Camps et al. (2011)	
GS7	838.0	140.0	^{40}Ar/^{39}Ar	831.8	78.8	6.7				Camps et al. (2011)	Camps et al. (2011)	
GS4	844.0	80.0	^{40}Ar/^{39}Ar	837.7	33.9	9.2				Camps et al. (2011)	Camps et al. (2011)	
GS3	875.0	26.0	^{40}Ar/^{39}Ar	868.5	39.2	11.6				Camps et al. (2011)	Camps et al. (2011)	
GS2	748.0	91.0	^{40}Ar/^{39}Ar	742.4	45.6	5.4				Camps et al. (2011)	Camps et al. (2011)	
(8) NW-USA (45.5°N/238.0°E)												
T5278	761.0	5.0	^{40}Ar/^{39}Ar	765.9	76.8	5.9	5.5	na	5	Fleck et al. (2014)	Hagstrum et al. (2017)	Lhuillier et al. (2017)
BL8113	761.0	5.0	^{40}Ar/^{39}Ar	765.9	87.4	3.2	6.1	0.7	5	Fleck et al. (2014)	Hagstrum et al. (2017)	Lhuillier et al. (2017)
T5153	773.0	5.0	^{40}Ar/^{39}Ar	778	7.8	5.5	4.1	na	5	Fleck et al. (2014)	Hagstrum et al. (2017)	Lhuillier et al. (2017)
BL9001	773.0	5.0	^{40}Ar/^{39}Ar	778	0.9	6.7				Fleck et al. (2014)	Hagstrum et al. (2017)	
4T104	869.0	6.0	^{40}Ar/^{39}Ar	875	−74.4	1.7	5.4	na	5	Fleck et al. (2014)	Hagstrum et al. (2017)	Lhuillier et al. (2017)
(9) Antarctica (−77.5°N/169.2°E)												
MC15	770.0	32.0	^{40}Ar/^{39}Ar	786.5	−88.5	8.1				Tauxe et al. (2004)	Tauxe et al. (2004)	
MC105	860	70.0	K-Ar$^{(conv)}$	na	−64.6	3.2	4.3	0.4	6	Armstrong (1978)	Lawrence et al. (2009)	Lawrence et al. (2009)
MC148	720.0	660.0	K-Ar$^{(conv)}$	na	69.6	10.7	7.0	0.5	6	Wilch (1991)	Lawrence et al. (2009)	Lawrence et al. (2009)
MC100	860.0	230.0	^{40}Ar/^{39}Ar	865.6	75.9	4.6				Lawrence et al. (2009)	Lawrence et al. (2009)	
MC139	880.0	80.0	^{40}Ar/^{39}Ar	885.7	−80.1	4.3				Tauxe et al. (2004)	Lawrence et al. (2009)	
(10) Mexico (18.44°N/264.92°E)												
TP	800.0	100.0	K-Ar$^{(conv)}$	na	87.3	5.7	8.4	1.6	4	Nelson and González-Caver (1992)	Alva-Valdivia et al. (2001)	Alva-Valdivia et al. (2001)
TS	800.0	100.0	K-Ar$^{(conv)}$	na	74.9	3.9	9.1	1.3	5	Nelson and González-Caver (1992)	Alva-Valdivia et al. (2001)	Alva-Valdivia et al. (2001)
CH	728.0	18.0	^{40}Ar/^{39}Ar	737.2			8.3	1.3	4	Ownby et al. (2007)		Michalk et al. (2010)
AZ	730.0	118.0	^{40}Ar/^{39}Ar	739.2	78.4	11.0	12.1	1.4	3	Ownby et al. (2007)	Michalk et al. (2010)	Michalk et al. (2010)
(11) Germany (50.2°N/6.8°E)												
SW	722.0	38.0	^{40}Ar/^{39}Ar	726.4	34.9	2.5	2.5	0.4	4	Singer et al. (2008)	Schnepp and Hradetzky (1994)	Schnepp and Hradetzky (1994)

Note. Recal. age, recalibrated age (according to ACs or FCs standards, see text); ^{40}Ar/^{39}Ar, Argon/Argon; K-Ar, potassium/Argon; VGP lat, virtual geomagnetic pole latitude; A95, radius of the 95% confidence circle about the calculated mean pole. We estimated it as the square root of dp × dm (see Khramov (1987)) which are the semi axes of the ellipse at 95% confidence level (calculate from equations 7.8 and 7.9 in Butler (1992)), VADM, virtual axial dipole moment; SD, standard deviation; Am^2, Ampere/meter^2; PI, paleointensity; na, not applied; Q_{PI}, quality of paleointensity data. All ^{40}Ar/^{39}Ar age errors are provided with 2σ, but K-Ar age errors are provided with 1σ. ^{conv} and ^{CG} refer to conventional and Cassignol-Gillot (Gillot & Cornette, 1986; Quidelleur et al., 2001) techniques that were use during K-Ar dating, respectively.

[a]Refer to VADM calculated from RPI data (Azores) after scaling them to absolute values (See Section 2.2.5. We use the Q_{PI} values as listed in the PINT database (Bono et al., 2022). The Q_{PI} values of the four Guadeloupean sites (G03, G02, G01, and GD01) and the Chilean site (QTW11-20), which are noted with an asterisk *, were newly assigned for this study. Also, we assigned Q_{PI} values for the Azores sites (designated with a **)).

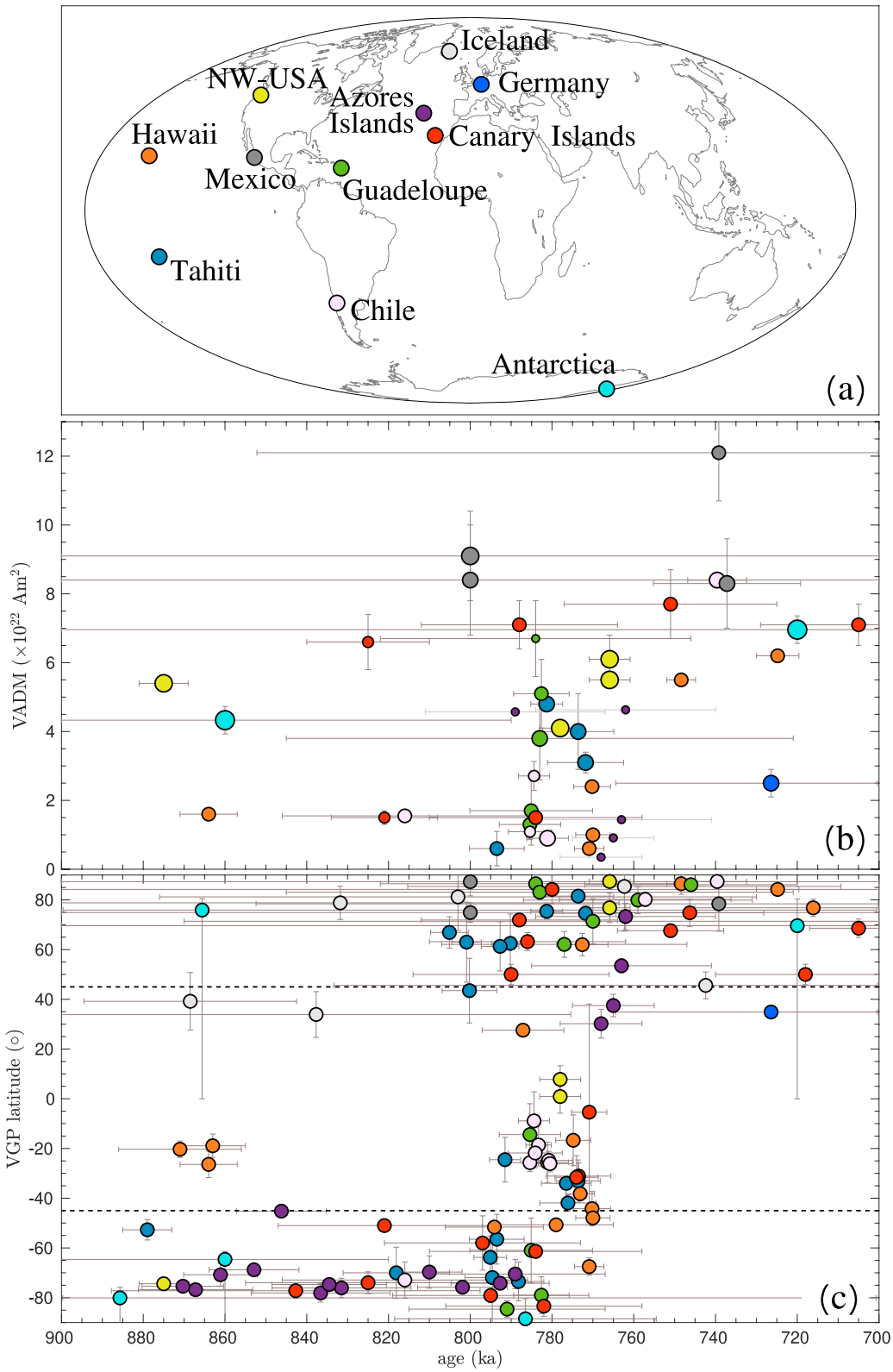
Iceland
NW-USA
Germany
Azores
Islands
Hawaii
Canary Islands
Mexico
Guadeloupe
Tahiti
Chile
Antarctica
(a)
VADM ($\times 10^{22}$ Am^2)
(b)
VGP latitude (°)
(c)
age (ka)

Figure 1.

McDougall, 1967). In addition to the traditional K-Ar approach, the K-Ar Cassignol-Gillot technique (Gillot & Cornette, 1986; Quidelleur et al., 2001), which applied to separated groundmass, is mentioned here. This technique is suitable for dating Quaternary volcanic rocks (Guillou et al., 1996; Quidelleur et al., 2001, 2003; Samper et al., 2007), with a detection limit being of 10% of the radiogenic Ar content (Quidelleur et al., 2001). For K-Ar age data assembled here (Table 1), four studies (Abdel-Monem et al., 1972; Armstrong, 1978; Nelson & González-Caver, 1992; Wilch, 1991) provided K-Ar ages using the conventional approach, whereas the remaining K-Ar ages were determined using the refined Cassignol-Gillot technique. However, we accept all K-Ar age data in this study because the available database is already sparse. Reported age uncertainties range from 3 to 660 ka, with 22 sites having age errors ≤5 ka, 30 in the range 5–10 ka, and 56 sites have errors greater than 10 ka. Age errors are larger in sites with K-Ar ages than in $^{40}Ar/^{39}Ar$ dated sites. This situation prevents from obtaining crucial information regarding the fast changes in the magnetic field during the reversal. Nevertheless, the age data are carefully checked, and any updates are taken into account. The $^{40}Ar/^{39}Ar$ method requires standards that are used to calibrate the quantity of ^{40}K that can be attributed to a specific amount of ^{40}Ar in an analysis. Five standards are typically used in the $^{40}Ar/^{39}Ar$ geochronology: FCs, ACs, Mklhb-I, GA-1550, and TCs (for details of these standards see, e.g., Renne et al. (1998)). In this study, all $^{40}Ar/^{39}Ar$ ages have been recalibrated using the equivalent ACs (1.1851 ± 0.0004; Schaen et al. (2020)) or FCs (28.201 ± 0.046; Kuiper et al. (2008)) standards using the Min et al. (2000) decay constant ($\lambda = 5.463 \pm 0.054 \times 10^{-10}$/year). This is another source of difference between our compilation and PINT, as the latter did not perform any recalibration on the $^{40}Ar/^{39}Ar$ ages. The original ages are listed alongside the calibrated ages in Table 1. The calibration is done using the following equation given by Renne et al. (1998):

$$Age_{\substack{recalculated\ at \\ 1.1851\ or\ 28.201\ Ma}} = \frac{1}{\lambda} \times \ln\left[\left(e^{\lambda \times Age_{reported}} - 1\right) \times R^{Age_{reported}}_{\times standard} \times R^{\times standard}_{AC\,or\,FCs} + 1\right]$$

Paleomagnetic directions amount to nearly 2.5 times the PI values. The scarcity of PI data is likely due to the challenges of obtaining reliable PI from lavas (see, e.g., Tauxe, 2010, for details). We do not set threshold values for statistical parameters of the gathered site-mean directions, which are the number of specimens (N) utilized to compute the mean direction, the 95% angle of confidence (α_{95}), and the precision parameter (k). A significant portion of volcanic data does not fulfill high statistical standards (see Table 1), which is to be expected when dealing with paleomagnetic data in a transitional field state. The 42 site-mean PI values were obtained by different methods, including: the double heating Thellier technique (Thellier & Thellier, 1959) with various modifications (Aitken et al., 1988; Coe, 1967; Tauxe & Staudigel, 2004); the Microwave approach (Hill & Shaw, 1999); Shaw method (Shaw, 1974) and its variants (e.g., Tsunakawa & Shaw, 1994); and the multispecimen technique (Dekkers & Böhnel, 2006). Beside absolute PI data, five relative PI data are available from the Azores (Ricci et al., 2020). These data are scaled to absolute values in this study, following the approach described in Section 2.2.5. The quality of the current PI data was evaluated using the quality of PI (Q_{PI}) metrics, which were first introduced by Biggin and Paterson (2014). The updated PINT database (Bono et al., 2022) increased these metrics from 8 to 10 criteria. In general, the criteria are based on age information, type and stability of remanent magnetization, rock magnetic properties, PI data (number of specimens, uncertainty, and reliability parameters), as well as its availability. The PINT database was used to score the sites of this study by Q_{PI}, with a notice that the Q_{PI} values for four sites from Guadeloupe and one site from Chile (see Table 1) were adjusted in this study. Additionally, Q_{PI} of the scaled intensity data from the five Azores sites was assigned in this study. These sites get a Q_{PI} score of 1/10 because, aside from the age-related information, they lack information on the other nine requirements. The Q_{PI} in the 42 sites have a range of 1/10–6/10, with a median value of 3/10. This suggests that the majority of PI data recording MBR have low Q_{PI} values. The highest Q_{PI} values for PI data come from Antarctica (Lawrence et al., 2009) and NW-USA (Lhuillier et al., 2017) sites, which have 6/10 and 5/10, respectively.

We use VADM and VGP parameters to represent intensity and directional changes, respectively, from our compilation of lava data over the past 900–700 ka. Here we consider the transitional polarity state by the commonly used range of VGP latitude values between +45° and −45°. Most of the sites between 900 and 800 ka have reverse

Figure 1. (a) Global distribution of volcanic data compiled from 11 regions for characterizing the evolution of the Matuyama-Brunhes reversal. Virtual axial dipole moment (VADM) and virtual geomagnetic pole (VGP) latitude for the past 900–700 ka are also plotted in (b) and (c), respectively. From 108 volcanic sites, 42 site-mean VADMs and 107 site-mean VGPs were collected. Note that age uncertainties are given at the 2σ level while the age errors of K-Ar age data (at the 1 σ level) are recalculated at 2σ level here. The two black dashed lines in panel (c) indicate VGP latitudes of ±45°. Errors extending outside the covered period (200 ka) are not fully displayed. The size of the circles in the VADM graph is dependent on the Q_{PI} values (See text and Table 1) with larger circles corresponding to higher Q_{PI} values.

polarity, and three sites have VADM of ~4–6 × 10^{22} Am^2, which are consistent with the stable Matuyama reverse polarity chron. Other sites, however, exhibit transitional (sites from Hawaii, Azores Islands, and Iceland) and normal (in Iceland and Antarctica sites) polarity directions throughout this time. Keep in mind that sites from Antarctica and Iceland have significant inaccuracies in their age and/or VGP data. The VADM value of one of the three transitional polarity locations in Hawaii (noted between 863 and 871 ka) was 1.6 × 10^{22} Am^2, indicating that the transitional field state occurred under low field strength.

VGP data show transitional polarity directions between ~795 and 770 ka in six volcanic regions: Tahiti, Hawaii, Guadeloupe, Chile, Canary Islands, and NW-USA. During this time, intensity decay was noted in Tahiti, Chile, Guadeloupe, Hawaii and the Azores. However, during this period, some sites from Tahiti, Guadeloupe, Canary Islands, and NW-USA have high intensities values. The transition stage lasts until ~760 ka, when two Azores sites still have VGP latitudes of ~30°N. Two thousand years later, at 762 ka, one Azores site has a VGP latitude of 73°N and VADM = 4.6 × 10^{22} Am^2, which is 60% of the present-day dipole moment (7.6 × 10^{22} Am^2), according to latest version of IGRF model (Alken et al., 2021). Only nine VADM data exist between 762 and 700 ka, six of which have a mean of 6.0 × 10^{22} Am^2, showing that the magnetic field has most likely stabilized. This can also be seen in the VGP data, where the majority of the data during this time period is of typical normal polarity. One site from the West Eiffel, Germany (Singer et al., 2008), with a calibrated $^{40}Ar/^{39}Ar$ age of 726 ka, exhibits unusual behavior, with transitional polarity state (VGP = 35°N) and low VADM (2.5 × 10^{22} Am^2). This anomalous behavior could, however, be connected to the site's significant 2σ age uncertainty of 38 ka. Due to large age errors and still insufficient data set, it is impossible to pin down the beginning and end of the MBR using solely lava locations. This necessitates the use of continuous sediment records.

2.2. Sediment Data

2.2.1. Compilation and Spatio-Temporal Distribution

During the data compilation procedure for sediments, we focus on records with magnetic field components on a time scale. Records with paleomagnetic data on a depth scale that clearly specify the SR and the depth at which the MBR occurred have also been compiled. In this case, linear interpolation was used to convert to a time scale considering constant depositional rate. Other cases in which data is only available on a depth scale are not taken into account. Therefore no paleomagnetic data from the MBD97 (Love & Mazaud, 1997) database has been considered. Paleomagnetic data that have been reported from deep-sea sediments, shallow-sea sediments, and lake sediments (including lacustrine deposits) are only considered during data compilation. We do not use paleomagnetic data reported from Loess deposits, because doubts have been raised about the ability of these sediments to record the magnetic field signal during reversals (Wang et al., 2014; Wu et al., 2016; Zhou et al., 2014). Regarding RPI data, we accept bulk magnetic properties, magnetic susceptibility (MS), anhysteretic remanent magnetization (ARM), and isothermal remanent magnetization (IRM), as normalization factors.

Under these selection criteria, we compiled 68 sediment records, of which 56 are deep-sea sediments and the remaining 12 are shallow-sea and lake sediments. Table 2 contains a list of these sediment data and the geographic distribution is shown in Figure 2a. The majority are located in three regions from the north-eastern hemisphere (North Atlantic, Western Equatorial Pacific, and North Pacific), which account for over 92% of the total. Note that this is in contrast to the lava sites distribution (see Figure 1a), where most of data are distributed in the western hemisphere. As illustrated in Figure 2a, the southern hemisphere contributes just a modest amount of data; data are not available in the southern half of South America, Africa, and Australia. A number of 28 sediment cores have full vector paleomagnetic data, 26 have only RPI, and the other cores have one or two magnetic field components.

Temporal distributions of sediment data are plotted in Figure 2b where the number of data are shown in 2 ka years bins. There are 13,068 declination, 13,454 inclination, and 16,897 intensity data points in total. Note that we only display data that have been accepted in this study. Between 760 and 800 ka, the period when the MBR was supposed to occur, almost 30% of the full-vector (declination, inclination, and RPI) field data (5,177) are concentrated. The North Atlantic region holds the majority of these data, with 10,067, 10,067, and 12,262 data for declination, inclination, and intensity, respectively, equally distributed over the studied period. These data account for ~74% of the whole data set. Most of the *N*. Atlantic data are distributed between 800 and 780 ka.

Journal of Geophysical Research: Solid Earth

10.1029/2022JB025286

Table 2
List of 68 Sediment Cores Evaluated in This Study

Code	Record	Lat. (°N)	Long. (°E)	Min age (ka)	Max age (ka)	Dating method	SR (cm/Kyr)	Sampling method	*D*/*I*/*F*	Accepted/ reason	Reference
North Atlantic											
EIDA	U1305	57.48	−48.50	0	1,181	$\delta^{18}O$	17.5	U-channel	*D*/*I*/*F*	No/RC	Mazaud et al. (2012)
EIDB	U1306	58.24	−45.64	0	2100,0	RPI + $\delta^{18}O$	15.0	U-channel	*D*/*I*/*F*	Yes	Channell et al. (2014)
EIDC	U1307	58.51	−46.40	4	2,266	POL + RPI	~5.5	U-channel	*D*/*I*/*F*	Yes	Mazaud et al. (2015)
SGDR	U1304	53.10	−33.50	0	1,500	$\delta^{18}O$	15.0	U-channel	*D*/*I*/*F*	Yes	Xuan et al. (2016)
CNAA	DSDP 609B	49.90	−24.20	777	825	POL	7.0	Discrete	*F**	No/DT	Hartl and Tauxe (1996)
CNAB	IODP U1308	49.90	−24.20	1	1,528	$\delta^{18}O$	7.3	U-channel	*D*/*I*/*F*	Yes	Channell et al. (2008)
NGDR	ODP 983	60.40	−23.60	500	900	OT-$\delta^{18}O$	11.3	U-channel	*D*/*I*/*F*	Yes	Channell et al. (1998); Channell et al. (2004); Channell and Kleiven (2000)
BJDR	ODP 984	61.40	−24.01	500	900	OT-$\delta^{18}O$	12.0	U-channel	*D*/*I*/*F*	Yes	Channell et al. (2004)
ORPH	U1302-03	50.10	−45.60	0	764	RPI + $\delta^{18}O$	14.0	U-channel	*D*/*I*/*F*	No/RC	Channell et al. (2012)
FNDR	ODP 980	55.50	−14.70	13	1,189	OT − $\delta^{18}O$	16.0	U-channel	*D*/*I*/*F*	Yes	Channell and Raymo (2003)
RKRG	MD95-2016	57.40	−30.80	762	802	$\delta^{18}O$	4.0	Discrete	*F*	Yes	Valet et al. (2019)
Western Equatorial Pacific											
CEBS	ODP 767B	4.80	124.00	759	794,0	$\delta^{18}O$	10.0	Discrete	*D*/*I*/*F*	No/RC	Oda et al. (2000)
SUSA	ODP 769A	8.80	121.30	760	790	$\delta^{18}O$	10.0	Discrete	*D*/*I*/*F*	Yes	Oda et al. (2000)
SUSB	ODP 769B	8.80	121.30	765	794	$\delta^{18}O$	10.0	Discrete	*D*/*I*/*F*	No/RC	Oda et al. (2000)
OJPA	KH73-4-7	7.70	164.80	32	1,138	POL + ESR + PAL	1.0	Core	*F*	Yes	Sato and Kobayashi (1989)
OJPB	KH73-4-8	−1.60	167.60	115	1,137	POL + ESR + PAL	1.0	Core	*F*	Yes	Sato and Kobayashi (1989)
OJPC	KH90-3-5	4.00	160.02	32	1,106	POL + $\delta^{18}O$	1.0	Core	*F*	Yes	Sato et al. (1998)
OJPD	805B	1.10	160.30	770	821	POL	2.0	Discrete	*F**	No/DT	Hartl and Tauxe (1996)
OJPE	804C	1.00	161.40	774	796	POL	1.0	Discrete	*F**	No/DT	Hartl and Tauxe (1996)
OJPF	807A	4.00	157.00	781	2,036	POL	nd	Discrete	*F*	No/DT	Kok and Tauxe (1999)
WPHS	MD97-2143	15.90	124.70	0	2,140	$\delta^{18}O$	2	Discrete	*D*/*I*/*F*	Yes	Horng et al. (2002); Horng et al. (2003)
WCBA	MD97-2140	2.10	141.80	568	1,465	POL	1.8	U-channel	*F*	No/DT	Carcaillet et al. (2003)
WCBB	MD98-2183	2.00	135.00	20	1,193	POL + MS + RM	2.0	Discrete	*F*	Yes	Yamazaki and Oda (2005)
WCBC	MD98-2185	3.10	135.00	9	2,256	POL + MS + RM	2.0	Discrete	*F*	Yes	Yamazaki and Oda (2005)
WCBD	MD98-2187	4.30	134.80	51	3,053	POL + MS + RM	1.0	discrete	*F*	Yes	Yamazaki and Oda (2005)
CRRG	MR1402-PC1	6.50	138.90	615	3,188	POL	0.1	Discrete	*D*/*I*/*F*	No/DT	Sakuramoto et al. (2017)
BANS	MD012380	−5.80	126.90	0	820	$\delta^{18}O$ + RPI+ ^{14}C	4.9	U-channel	*F*	No/RC	Huang et al. (2009)
North Pacific											
HSRA	NGC69	40.00	175.00	9	881	RM	1 0.0	Discrete	*F*	No/RC	Yamazaki (1999)
HSRB	KR0310-PC1	35.20	175.00	0	1,600	RM	1.2	Discrete	*F*	Yes	Yamazaki and Kanamatsu (2007)

Journal of Geophysical Research: Solid Earth

10.1029/2022JB025286

Table 2
Continued

Code	Record	Lat. (°N)	Long. (°E)	Min age (ka)	Max age (ka)	Dating method	SR (cm/Kyr)	Sampling method	*D*/*I*/*F*	Accepted/ reason	Reference
HSRC	SO202-1	38.00	164.50	6	942	$\delta^{18}O$ + POL	2.1	Discrete	*I*/*F*	Yes	Korff et al. (2016)
HSRD	NPGP1401-2A	32.00	178.60	2	1,072	Ba/Ti + RM	0.7	Discrete	*F*	Yes	Shin et al. (2019)
NJGY	RC10-167	33.00	150.40	3	963	POL + RPI	2.1	Discrete	*D*/*I*/*F*	No/RC	Kent and Opdyke (1977); Meynadier et al. (1995)
OSBS	OB	34.80	135.60	753	794	DTM	60.0	Discrete	*D*/*I*/*F*	Yes	Hyodo et al. (2006); Hyodo and Kitaba (2015); Maegakiuchi et al. (2016)
CHBA	YGC	35.40	140.10	768	787	$\delta^{18}O$ + TPH	89.0	Discrete	*D*/*I*	Yes	Suganuma et al. (2015)
CHBB	YT	35.30	140.10	770	774	$\delta^{18}O$ + TPH	89.0	Discrete	*D*/*I*/*F*	Yes	Haneda et al. (2020)
CHBC	CBCS	35.30	140.10	748	794	$\delta^{18}O$ + TPH	89.0	Discrete	*D*/*I*/*F*	Yes	Haneda et al. (2020)
CHBT	CHBT	35.38	140.31	769	780	$\delta^{18}O$ + TPH	18.0–30.0	Discrete	*D*/*I*/*F*	Yes	Oda et al. (2022)
Antarctica											
WKBA	1101	−64.40	−70.30	700	1,100	POL + MS	8.8	U-channel	*F*	Yes	Guyodo et al. (2001)
WKBB	PC20	−65.00	143.80	0	780	RPI	0.6	U-channel	*I*/*F*	Yes	Macrì et al. (2005)
WKBD	CADO	−64.90	144.80	2	800	RPI	4.4	U-channel	*D*/*I*/*F*	Yes	Macrì et al. (2010)
Eastern Northern Pacific											
GUAD	GUAD	37.30	−121.90	9	1,081	POL	37.0	Discrete	*I*	No/DT	Mankinen and Wentworth (2016)
CCOC	CCOC	37.30	−121.90	10	784	POL	37.0	Discrete	*I*	No/DT	Mankinen and Wentworth (2016)
STPK	STPK	37.30	−121.90	24	784	POL	37.0	Discrete	*I*	No/DT	Mankinen and Wentworth (2016)
BJCF	ODP 1010	30.00	−118.10	19	2,036	POL + MS	1.3	U-channel	*F*	Yes	Hayashida et al. (1999); Leonhardt et al. (2009)
MFZA	ODP 1021.A	39.10	−126.20	13	1,562	POL + MS	~4.0	U-channel	*F*	Yes	Guyodo and Valet (1999); Leonhardt et al. (1999)
MFZB	ODP 1021.B	39.10	−126.20	0	4,500	POL + MS	~4.0	Discrete + U-channel	*D*/*I*/*F*	No/TR	Valet et al. (2020)
Mediterranean											
SIST	LC07	38.20	10.10	754	1,033	POL + RM + OT − $\delta^{18}O$	2.3	U-channel	*F*	Yes	Dinarès-Turell et al. (2002)
HSSB	HS	39.31	16.34	780	793	$^{40}Ar/^{39}Ar$	35.0	Discrete	*D*/*I*/*F*	Yes	Sagnotti et al. (2014); Sagnotti et al. (2016)
COBS	CB	39.31	16.34	764	793	$\delta^{18}O$	27.0–94.0	Discrete	*D*/*I*	Yes	Macrì et al. (2018)
LKOH	ICDP 5045-1	41.05	20.72	2	1,293	TPH	25.0	Discrete	*I*/*F*	No/RPI	Just et al. (2019)
Equatorial Indian Ocean											
MDVA	MD90-0940	−5.60	61.70	108	1,954	OT − $\delta^{18}O$	1.3	Discrete	*D*/*I*/*F*	Yes	Meynadier et al. (1994)
MDVB	MD90-961	5.06	73.88	738	847	OT − $\delta^{18}O$	4.8	Discrete	*D*/*I*/*F*	Yes	Valet et al. (2014)
MDVC	MD90-949	2.10	76.10	750	800	OT − $\delta^{18}O$	2.8	Discrete	*F*	Yes	Valet et al. (2016); Valet et al. (2019)

Journal of Geophysical Research: Solid Earth

10.1029/2022JB025286

Table 2
Continued

Code	Record	Lat. (°N)	Long. (°E)	Min age (ka)	Max age (ka)	Dating method	SR (cm/Kyr)	Sampling method	*D*/*I*/*F*	Accepted/ reason	Reference
Eastern Equatorial Pacific											
CPIA	ODP 848-851	2.00	−110.00	34	4,035	POL + GRAPE	∼2.0	Discrete	*F*	Yes	Valet and Meynadier (1993)
CPIB	ODP 851	2.00	−110.60	0	4,300	POL + δ^{18}O	∼2.0	Discrete + U-channel	*D*/*I*/*F*	No/TR	Valet et al. (2020)
CPIC	U1335	5.30	−126.30	0	8,200	POL	∼0.5	U-channel	*D*/*I*/*F*	No/DT	Yamazaki and Yamamoto (2018)
Caribbean sea											
CASA	CAS16-24PC	15.10	−59.60	3	1,148	POL + RPI + δ^{18}O	1.7	Discrete + U-channel	*D*/*I*/*F*	Yes	Bieber et al. (2021)
CASB	IODP U1396	16.50	−62.50	1.9	4,516	POL + δ^{18}O	2.0–3.0	U-channel	*D*/*I*	No/UD	Hatfield et al. (2021)
Mid-latitude North Atlantic											
BRSA	606A	37.00	−37.00	773	792	POL	3.0	Discrete + U-channel	*D*/*I*/*F*	No/DT	Clement and Kent (1987); Hartl and Tauxe (1996)
BRSB	ODP1063	33.70	−57.60	500	798	RPI + δ^{18}O	25.0	Discrete + U-channel	*D*/*I*/*F*	No/TR	Channell et al. (2012)
Southern Atlantic											
AGBS	KS752	−37.80	−38.10	600	1,000	POL + MS	nd	Discrete	*F*	No/RPI	Valet et al. (1994)
Russian Arctic											
EGYG	ICDP-5011	67.50	172.00	0	3,588	POL + STR	4.0–5.0	Discrete + U-channel	*I*	Yes	Nowaczyk et al. (2013)
Equatorial Atlantic											
PFZA	665A	3.00	−20.00	770	817	POL	2.0	Discrete	*F**	No/DT	Tauxe et al. (1989) Hartl and Tauxe (1996)
PFZB	664D	0.10	−23.30	770	807	POL	4.0	Discrete	*F**	No/DT	Valet et al. (1989); Tauxe et al. (1989)
Central Pacific											
CPFB	P226	2.90	−169.60	41	780	POL	0.6	Discrete	*F*	No/DT	Yamazaki et al. (1995)
BISM	KK78-10-30	18.90	−160.30	601	1,785	POL	2.0	U-channel	*I*/*F*	No/DT	Laj et al. (1996)
Central Europe											
ZAHJ	ZAHJ	49.7	16.9	754	804	POL	0.5–1.0	Discrete	*D*/*I*/*F*	No/DT	Ucar et al. (2021)
Sub-Antarctic Indian Ocean											
WMID	V16-58	−46.50	31.30	767	790	POL	2.5	Discrete	*D*/*I*/*F*	No/DT	Clement and Kent (1991); Kent and Schneider (1995)

Note. Lat, latitude; Long, longitude; Min age, minimum age; Max age, maximum age; OT−δ^{18}O, Orbitally tuned oxygen isotope; RPI, relative paleointensity; POL, polarity; MS, magnetic susceptibility; RM, rock magnetic; DTM, diatom; TPH, tephrachronology; GRAPE, gamma-ray attenuation porosity evaluator; STR, stratigraphy; Ba/Ti, barium/titanium ratio; SR, sedimentation rate; *D*/*I*/*F*, declination/inclination/intensity-components of the magnetic field; RC, regional consistency; DT, dating; TR, timing of reversal; UD, unreliable direction (applies for record IODP U1396 from Caribbean Sea). Sites DSDP 609B, 805B, 804C, 665A, and 664D provide full-vector field information (D/I/F), but we compile the F component from Ziegler et al. (2011), as indicated by the * in the *F* component for those sites. We did not construct the *D* and *I* components of these sites because they are only available on the depth-scale.

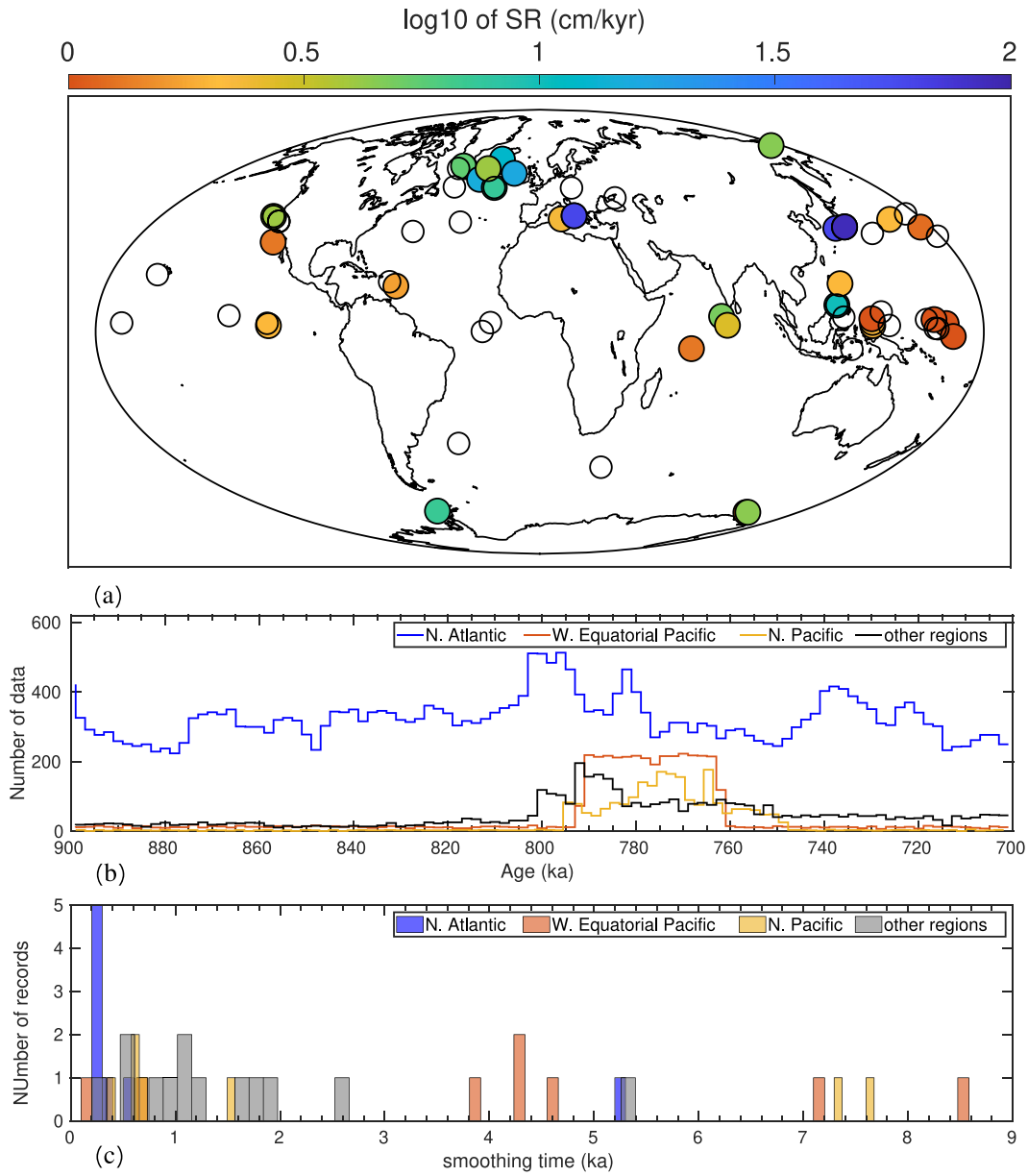

Figure 2. (a) Geographic distribution of 68 sediment records covering the Matuyama-Brunhes reversal. Thirty-eight records were accepted (marked by filled circles) while the rest (marked by open circles) were not accepted for our analyses (see Section 2.2.6). The accepted records' sedimentation rate distribution is depicted in (a) using a logarithmic color scale. The temporal distributions of the three magnetic field components (declination, inclination, and relative paleointensity) of the accepted sediment records are shown in (b). The majority of the data comes from three regions: the North Atlantic, Western Equatorial Pacific, and North Pacific, which are displayed separately from the other regions. The smoothing time values computed from the accepted sediment records are shown in a histogram (c). Note that smoothing time of record CAS16-24PC1 which is 18.8 ka is not included here.

The Western Equatorial Pacific is the second largest data-rich region, with data highly concentrated between 790 and 760 ka. It is worth noting, however, that it only amounts to 13% of the North Atlantic data and 9% of the whole data set. In the North Pacific, like the Western Equatorial Pacific, the majority of the data are centered between 780 and 760 ka. The rest of the regions (Antarctica, Eastern Northern Pacific, Mediterranean, Equatorial Indian Ocean, Eastern Equatorial Pacific, Caribbean Sea, and Russian Arctic) together only have 947 declination, 1,251 inclination, and 2,137 intensity data points. The larger part of these data fall into the Brunhes chron, more precisely between 800 and 700 ka.

2.2.2. Timescale Reliability and Updates

The gathered sediment records were dated using a variety of methods. We did not consider records that were dated purely by comparing the magnetic field direction to a reference record of known age derived from global or local data sets, because this method is not independent of the magnetic field variations that we want to investigate here. Polarity reversals (or magnetostratigraphy) and RPI correlation, are two other dating methods that depend on the magnetic field. In the polarity reversal method (POL), conversion from the depth-scale to the age-scale is generally performed by comparing the directional data of a specific record to one of the geomagnetic polarity timescale references (Cande & Kent, 1995; Gradstein et al., 2012; Hilgen, 1991; Shackleton et al., 1990). The conversion is carried out by assuming a constant SR and employing one or a few tie points. The reference in the RPI dating method is a regional or global RPI stack or model, such as SINT-800 (Guyodo & Valet, 1999), PISO-1500 (Channell et al., 2009), or PADM2M (Ziegler et al., 2011). In RPI dating, the timescale is derived from a large number of tie points, which is typically greater than in the POL approach, and it does not assume constant SR along the record. A total of 46 records were dependently dated, with 37 using POL and 9 using RPI dating (Table 2). Seventeen of the 37 POL age cores have only employed the POL method. Knowing the age of the MBR is required for POL dating, as this age is used as a primary (and in some cases unique) tie point. Therefore we do not include these 17 records in our following analyses, where we aim for independent estimates of MBR timing and duration, but keep them in our compilation for potential future use. The remaining 20 records combine POL with other dating methods and we include them. Moreover, we retain the 9 RPI-dated records since they do not require the MBR age and use more tie points. Although RPI does not vary synchronously over the globe, it is clearly influenced by dipole changes (see e.g., M. C. Brown et al., 2018; Korte et al., 2019) which might justify the age determination by this method dependent on magnetic field changes.

The preferable dating methods use features that are not tied to the Earth's magnetic field, which we call independent properties. The oxygen isotope (δ^{18}O) method, which was used on 29 of the 68 sediment cores, is the most common independent method. Global δ^{18}O stacks can be used to establish the paleoclimate by combining the mean time series of δ^{18}O data from numerous places throughout the world. SPECMAP (Imbrie et al., 1984) that covers the last 750 Kyr, S95 (Shackleton et al., 1995) that covers the last 6 Myr, and LR04 (Lisiecki & Raymo, 2005) that covers the last 5.3 Myr, are examples of such stacks. The age model of these stacks was built through orbital tuning; consequently, one may date a record by comparing δ^{18}O data to one of these stacks. The highest resolution is given by LR04, because it was created using 57 benthic δ^{18}O records published from globally well-distributed (in latitude, longitude, and depth) sites from the Atlantic, Pacific, and Indian Ocean. Its age model was determined by aligning the δ^{18}O stack with an ice model based on summer insolation at 65°N on the 21st of June (Lisiecki & Raymo, 2005). No modifications were done to sediment cores having LR04-assigned age data. For records that used SPECMAP and S95, conversion of their age to the LR04 age model can be done using the conversion relation available online (https://lorraine-lisiecki.com/LR04_age_conversion.txt). It is worth noting that a 5-Myr probabilistic stack was created from 180 δ^{18}O records, and can be used for dating (Ahn et al., 2017). However, because it was not used in any of the assembled records, we used LR04 and did not convert all data to this probabilistic stack. In addition to δ^{18}O, a total of 13 cores have been dated by comparing their rock magnetic properties, such as MS, S_{ratio}, ARM, and ARM/MS, to one of the δ^{18}O reference records or stacks. Other independent dating techniques, such as palaeontology (2 records), electron spin resonance (2), stratigraphy (1), tephrostratigraphy (4), diatom studies (1), gamma-ray attenuation porosity evaluator (1), and barium/titanium (Ba/Ti) ratio (1), have been utilized. We cannot go into details here, but we accepted all of these records.

During data compilation, published updates on the original age scale have been applied for four records (MD97-2143, OB, RC10-167, and HS), see supplement for details.

2.2.3. Temporal Resolution

In different aquatic environments, sediments are deposited at various SR. Deep-sea sediments have generally the poorest resolution, with typical SR on the scale of 1 cm/Kyr. Coastal ocean and shallow sea sediments have resolutions of a century to a millennium (10 cm/Kyr), whereas lake cores have resolutions of a decade to a century (100 cm/Kyr). The SR in the compiled records (Table 2) ranges from 0.5 to 89 cm/Kyr, with 40 records having SR $<$ 5 cm/Kyr, 4 having SR range 5–10 cm/Kyr, and 22 records having SR $\geq$ 10 cm/Kyr, that is, more than half of all the sediments data are of low resolution. There are two records (807A and KS752) without SR information provided. Regarding only the accepted records (which are 38): 22 records have SR $<$ 5 cm/Kyr; 3 in the range 5–10 cm/Kyr; and 13 records have SR $\geq$ 10 cm/Kyr. This indicates that there are no systematic differences in

SR between accepted and non-accepted records. The SR distribution is shown in Figure 2a, where we can see that North Pacific and Mediterranean records have the highest SR, and the maximum SR value of 89 cm/Kyr is found in three shallow marine-records (YGC, YT, and CBCS) from the North Pacific. The second largest SR, in the range of 25–60 cm/Kyr, are found in three Mediterranean records: the lacustrine section HS; shallow-marine sediment record CB, and lake record International Continental Scientific Drilling Program (ICDP) 5045-1. North Atlantic records have semi-uniformly high SRs, mostly around ≥10 cm/Kyr. The data from the Western Equatorial Pacific, on the other hand, show the lowest SR, which does not surpass 3 cm/Kyr, with the exception of three cores (ODP 769B, ODP 769A, and ODP 769B, SR = 10 cm/Kyr).

The temporal resolution of a sediment record is also influenced by the sampling method. U-channel and pass-through measurements lead to stronger smoothing of the signal than measurements on discrete samples. We assessed the temporal resolution of the compiled records by performing smoothing spline analysis (Panovska et al., 2012). This analysis provides estimates of the smoothing time (*T*s), which is the length of time that can be resolved in a sediment record. It is performed on each magnetic field component separately and can also help to assess the random uncertainty in the records. To perform the analysis, a prior *T*s value, which represents a threshold value for the time resolution during the spline analysis is required. We determine it from the SR and lock-in depth; SR values are used as listed in Table 2 while the lock-in depth is set to 10 cm for all sediment records. After obtaining a spline model of a given component, the *T*s is determined by estimating the full width at half maximum height of a resolving kernel that diagnoses the degree of smoothing inherent in the spline model (for more information see Panovska et al., 2012). We calculated an average *T*s for each record using smoothing spline analysis on 79 individual components established from the 38 acceptable sediment records. An example of the smoothing spline analysis is given in Supporting Information S1 (Figure S2). The distribution of the *T*s values is presented in Figure 2c. The resultant *T*s values range from 0.2 to 18.8 ka, with the median being ∼1.0 ka. The longest smoothing time (18.8 ka) was calculated from the Caribbean Sea record (CAS16-24PC). We note that, for the time range 900–700 ka, there are only 18 data points in this record. We found no significant changes in the resultant *T*s values when we decreased the lock-in depth parameter for this record to 0 or 5 cm. Except for this record, all analyzed records have *T*s < 10 ka, 25 have *T*s < 2 ka, and 18 records have *T*s ≦ 1 ka. We may deduce from the temporal resolution analyses that ∼50% of the sediment records selected in this study can capture magnetic field behavior during the MBR with a resolution better than 1 ka. It should be noted that the majority of the high resolution records are from the North Atlantic region.

2.2.4. Declination Orientation

We ascertain if the declination component in the records is azimuthally oriented. Since we are dealing with two antipodes polarities, median declination has to be south and north during the Matuyama reverse and Brunhes normal polarity chrons, respectively. Records that do not match this requirement are rotated in this study. In order to achieve this, mean average of the declination data over the two chrons were calculated, eliminating data of transitional polarity (VGP latitude between +45° and −45°). After that, the declination values are rotated, so as to have ∼180° and ∼360° median declination over Matuyama and Brunhes chrons, respectively. This approach is quite comparable to earlier ones (M. C. Brown et al., 2018; Panovska et al., 2021). Here, four records (ODP 980, ODP 984, MD97-2143, and CADO) were rotated. Figure S3 in Supporting Information S1 provides an example of the rotation process for record ODP 984.

2.2.5. Scaling of RPI Data

RPI values were estimated using different normalization factors: ARM, MS, and IRM. To scale RPI data, we must compare them, ideally to PI values from nearby volcanic data of known age, or to a calibrated stack or model constructed from RPI records (e.g., SINT-800, PISO-1500, PADM2M). The volcanic data are too sparse in the past 900–700 ka, as seen in Figure 1. We chose to use the 2,000 ka paleomagnetic axial dipole moment model PADM2M (Ziegler et al., 2011) that is built from 96,032 absolute and relative PI data obtained from archeomagnetic, igneous, and sedimentary archives.

Scaling was done by the approach described by M. C. Brown et al. (2018), using:

$$F_{rescale} = F_{RPI} / M_{RPI} * M_p, \quad (1)$$

where $F_{rescale}$ is the rescaled RPI data at each time step of a record, F_{RPI} is the RPI data at each time step, M_{RPI} is the median RPI over the full time range of the input sediment record, and M_p is the median absolute PI over

the time range of the sediment record, obtained from PADM2M. In order to convert VADM to intensity at each sediment core geographic location, we use the equation (Tauxe, 2010)

$$F = \mathrm{VADM}\mu_0/\left(4\pi a^3\right)\sqrt{1+3cos^2\theta}, \quad (2)$$

where a is the average radius of the Earth, μ_0 is the permeability of free space, F is absolute PI, and θ is the geographic co-latitude. We investigated scaling the sediment records across a 900–700 ka segment in addition to the full length. With the exception of one Balkan record (ICDP5045-1), the scaling results were nearly identical in both timeframes (Figure S4 in Supporting Information S1). When employing the full-length timescale, the M_P/M_{RPI} ratio for this record is 92.1, whereas using the 900–700 ka segment yields a ratio of 19.5. Except for ICDP5045-1, RPI data of all records are scaled over the full period covered by the records.

2.2.6. Regional Consistency of Sediments

After the dating check and RPI scaling, we have further selected the sediment records to ensure a high-quality, consistent data set for our investigation of the MBR. Three aspects are considered in this evaluation process: (a) regional consistency, (b) timing of the polarity transition, and (c) range of the scaled intensity values. Several regions contain more than one record, located within relatively close distances, so that similar geomagnetic variations are expected (e.g., Korte et al., 2019). We rejected records that display clearly different behavior from the others in regional proximity, as the credibility of the recovered paleomagnetic signal and/or the ages have to be questioned. Rejection was made also based on the polarity transition's timing: records that show a polarity reversal in VGP latitude at periods that are strongly different from all others were not considered in the following analysis. Records with very unusual intensity values are also discarded since they may indicate that the normalization might be insufficient and, for example, some climatic influences were not removed. It is not possible to define strict criteria because we do not know how irregular the magnetic field was around the MBR. Our decisions therefore are somewhat subjective based on current understanding of the reversal. Our choices are described in detail below, illustrated by plots of the time series of intensity (Figure 3) and direction (Figure 4), expressed by VADM and VGP latitude, of the records combined according to their regional distribution (Table 2).

In comparison to the rest of the North Atlantic records (Figures 3a and 4a), we observe that sites U1305 (Mazaud et al., 2012) and U1302-03 (Channell et al., 2012) show different VADM and VGP behavior. When three cores of U1305 were examined in detail (see Channell, 2017), hole-to-hole variations were noted. Two other records, U1304 and U1306, have similar hole-to-hole differences (Channell, 2017), but their VGP curves are not substantially different from the rest of the region's records. Note that Site U1305 was compared with Sites U1306 and U1307 (Text S2 in Supporting Information S1), as all three are from Eirik Drift and are ~70 km apart. The only instance for the Labrador Sea is Site U1302-03, which spans 764 ka (Channell et al., 2012). Its paleomagnetic results are inconsistent with the North Atlantic record, but agree with Site U1305. Nevertheless, we reject these two sites from the North Atlantic data collection. Record ODP1063 from the Mid-Latitude North Atlantic area is also not accepted, because the primary polarity transition is seen at ~762 ka (Figure 4j). From the Southern Atlantic, RPI data of core KS752 (Valet et al., 1994) had a significant problem that the natural remanent magnetization (NRM)/(ARM) and NRM/MS ratios are not the same, implying that it is characterized by non homogeneous magnetic mineralogy content. Therefore, we do not consider the VADM data (Figure 3k) derived from this core.

For the Pacific, according to the regional consistency and intensity range criteria, records ODP 767B (Oda et al., 2000) and MD012380 (Huang et al., 2009) from the Western Equatorial Pacific have distinct behavior and/or abnormal intensity values at 770–760 ka and 820–810 ka, and have been rejected (Figure 3b). We chose 769A from the two Sulu Sea holes (ODP 769A and 769B; Oda et al., 2000) because it is more consistent with other records of the region. The VADM curve of records NGC69 (Yamazaki, 1999) and RC10-167 (Kent & Opdyke, 1977; Meynadier et al., 1995) are different from rest of North Pacific records (Figure 3c) and therefore not considered. Record ODP1021.B (Valet et al., 2020) from the Eastern North Pacific has two main intensity lows, at ~825 ka and ~730 ka (Figure 3e). From the VGP latitude (Figure 4e), the main polarity transition occurred at ~730 ka. We reject this record since the time is very different from the widely accepted ages of the MBR (Channell et al., 2010; Shackleton et al., 1990; Singer et al., 2019; Valet et al., 2014). Similarly, record ODP851 from the Eastern Equatorial Pacific is discarded because its VADM and VGP data (Figures 3h and 4h) indicate the MBR at ~730 ka (Valet et al., 2020).

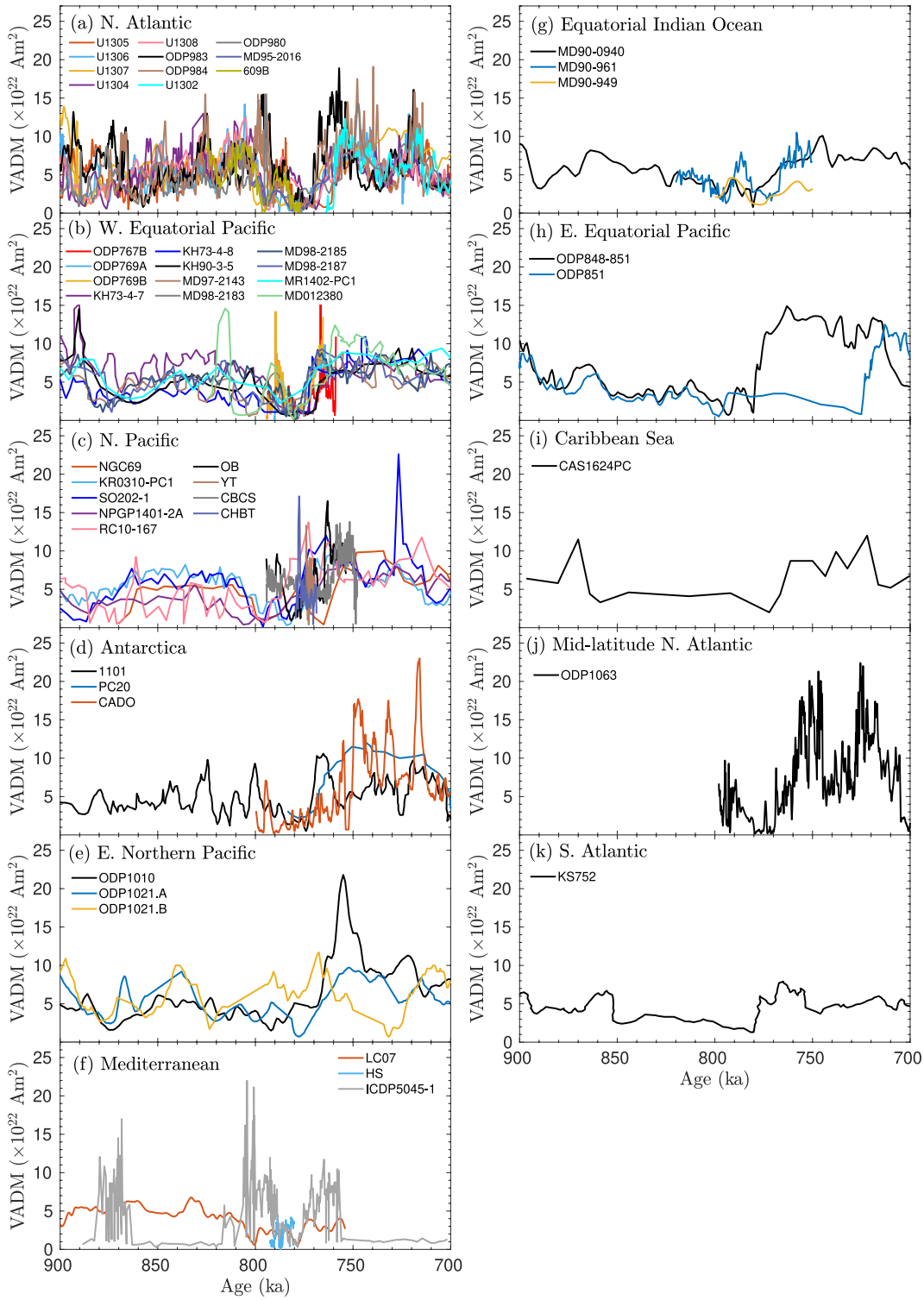

Figure 3. Virtual axial dipole moment curves of eleven regions (a–k) created from 49 individual record in the interval 900–700 ka with accepted time scales.

In the Mediterranean, we notice that record ICDP5045-1 from the Balkan (Just et al., 2019) (Figure 3f) has distinct behavior in comparison to records HS and LC07 (from Italy), which are located ~700 km west from it. VGP latitude of the ICDP5045-1 is also different from HS and LC07 (Figure 4f), hence we do not accept it.

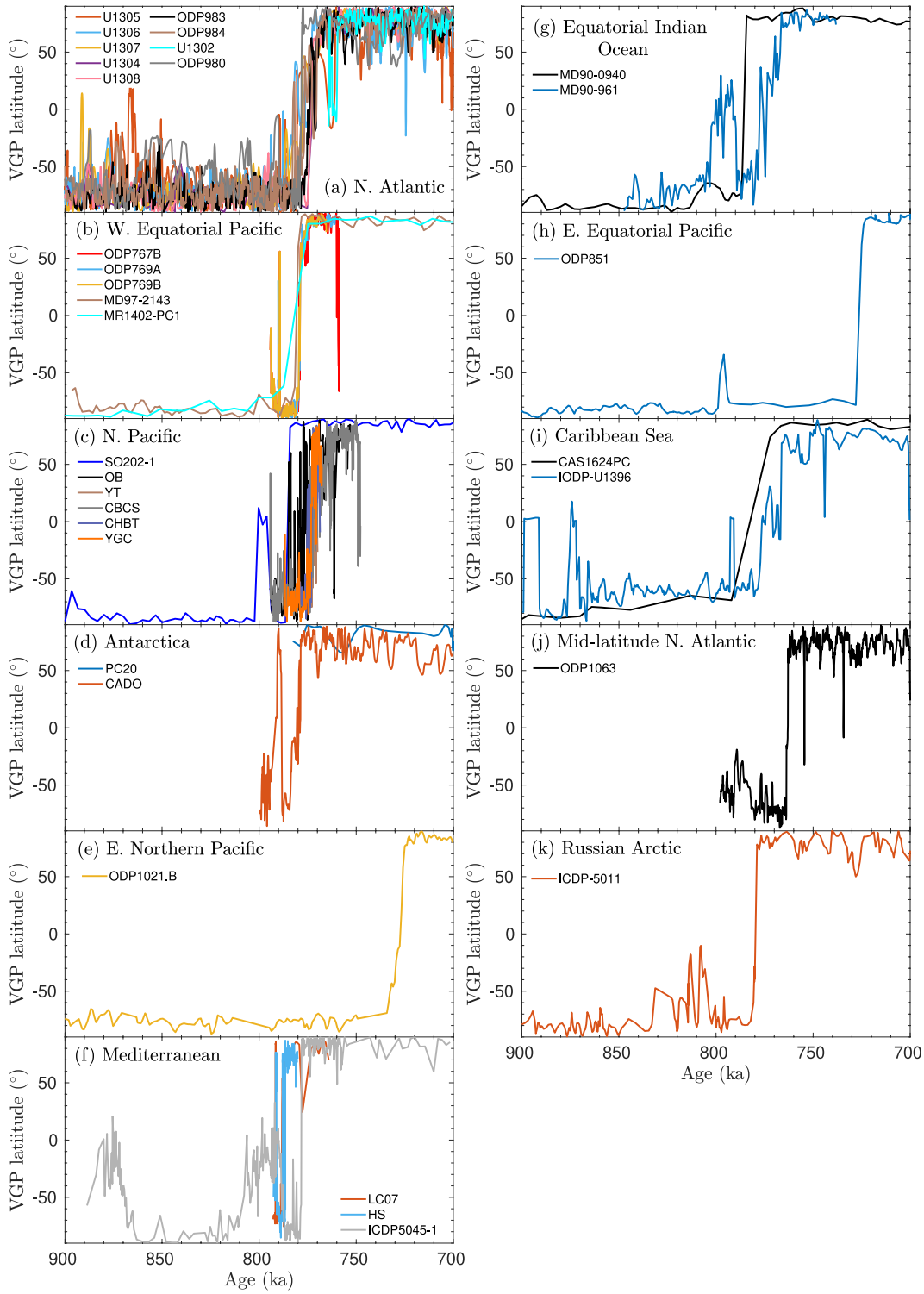

Figure 4. Curves of virtual geomagnetic pole latitude constructed from 33 records gathered from eleven regions (a–k) with accepted time scales.

The long Integrated Ocean Drilling Program U1396 record from the Caribbean Sea (Hatfield et al., 2021) is not accepted due to the poor paleomagnetic data quality of unit 2a, which includes the time of interest, as described in the original paper. This might be evident in the VGP curve derived from this record (Figure 4i). The main polarity transition for record ICDP-5011 from Lake El'gygytgyn, East Russian Arctic, is at ~780 ka (Nowaczyk

et al., 2013), which is consistent with other investigated regions. Although Nowaczyk et al. (2013) pointed out that there is no evidence for geomagnetic excursions during the Brunhes chron, we accept this record because the MBR appears to have been faithfully recorded.

3. Global Characteristics of the MBR

3.1. VADM Stack

To explore the stability of the magnetic field strength during the MBR, we create a set of regional VADM stacks and one global stack. In the regional stacks, our input curves are accepted records (which are 35) while the global stack was then built from these regional stacks. We should point out that individual records were not temporally aligned prior to establishing regional stacks; instead, we used their individual ages (see Section 2.2.2). This strategy differs from the commonly used approach (Channell et al., 2009; Guyodo & Valet, 1999; Laj et al., 2004; Valet et al., 2005) to align all records with a master record, which results in an average curve with lower uncertainty. However, some true variability of the non-dipole field may be lost by this process, and we do not employ this technique here.

VADM regional and global stacks were calculated by a bootstrap resampling technique where the data are resampled 5,000 times. VADM values of individual records from same region are combined into one data set. From this data set, 5,000 realizations are obtained by bootstrapping. For each of these realizations, a smoothing spline fit is obtained. The mean of these 5,000 fits is then calculated and produced at 500-year time steps, and this mean represents regional VADM stack. Confidence interval of each regional VADM stacks is provided at 2σ level. Seven regional VADM stacks were constructed using this approach (Figure 5a). Uncertainties for the regional stacks are not shown to avoid cluttering the figure. Indications for the uncertainties come from the comparison of the individual curves in Figure 3. Note that the bootstrap uncertainties may depend on the number of records and might not be fully reliable. In the western hemisphere, two regions (the Eastern Equatorial Pacific and the Caribbean Sea) each have only one acceptable record (Figures 3h and 3i). These two regions were not subjected to bootstrap analysis; instead, we kept their original VADM data and treated them as representative of the two regions. We maintain them because sediment records from the western hemisphere are few (Figure 2a). A global VADM stack with its 95% confidence interval was then generated by bootstrap resampling of the regional VADM stacks and the two representative regions, as shown in Figures 5a–5c. Note that the resampling does not take the age uncertainties of individual records into account, so that the confidence interval likely underestimates the true uncertainty. A global stack can also be build from all individual VADM data points of the 35 accepted records. However, the resulting curve appears to be biased toward the regional North Atlantic and Western Equatorial Pacific stacks, which are the most intensively covered regions (see Figure S5 in Supporting Information S1). We consider the stack based on regions as more representative for the global VADM variations.

The comparison of the regional stacks (Figure 5a) shows that the North Atlantic, North Pacific, and Antarctic stacks have the highest resolution, while the Western Equatorial Pacific, Eastern Equatorial Pacific, and Caribbean sea have the lowest resolution. The resolution is determined by the SR and the quantity of input records, among other factors. At ~820 ka, most of the regional stacks reveal a gradual decline in VADM. In addition, all regions experienced two major VADM drops at ~800–790 ka and 780–775 ka. Higher field intensity of different magnitude is recorded between these two minima, with the highest intensity being observed in the East Indian Ocean stack. The rates of magnetic field decay and growth vary between the curves during the entire 900–700 ka interval. For example, regions of the North Pacific, Mediterranean, and Eastern Equatorial Pacific display rapid intensity declines between 810 and 800 ka, whilst the North Atlantic stack shows more gradual decay. The magnetic field intensity increased rapidly after 775 ka, reaching generally higher levels than prior to 775 ka. This quick growth may be seen in the Eastern Equatorial Pacific curve, where the magnetic field intensity doubled in less than 1 ka. The rest of the regions display rapid growth as well.

The global VADM stack (Figures 5a–5c) shows a small VADM drop at ~820 ka (to 4.2×10^{22} Am^2), but the field increased back to its pre-820 ka VADM after 10 Kyr. Then, between 810 and 795 ka, the magnetic field intensity gradually decreased until it reached 3.7×10^{22} Am^2. After a short increase, the decrease to the lowest values observed in our stack is seen at 780 ka, with the VADM dropping to $\sim 2 \times 10^{22}$ Am^2. After 780 ka, the axial dipole moment rises steeply and only ~23 Kyr later (at 757–750 ka) the field reached $\sim 10 \times 10^{22}$ Am^2. This broad peak is about double as high as the values observed in the period 900–810 ka. A comparison of our new stack to some

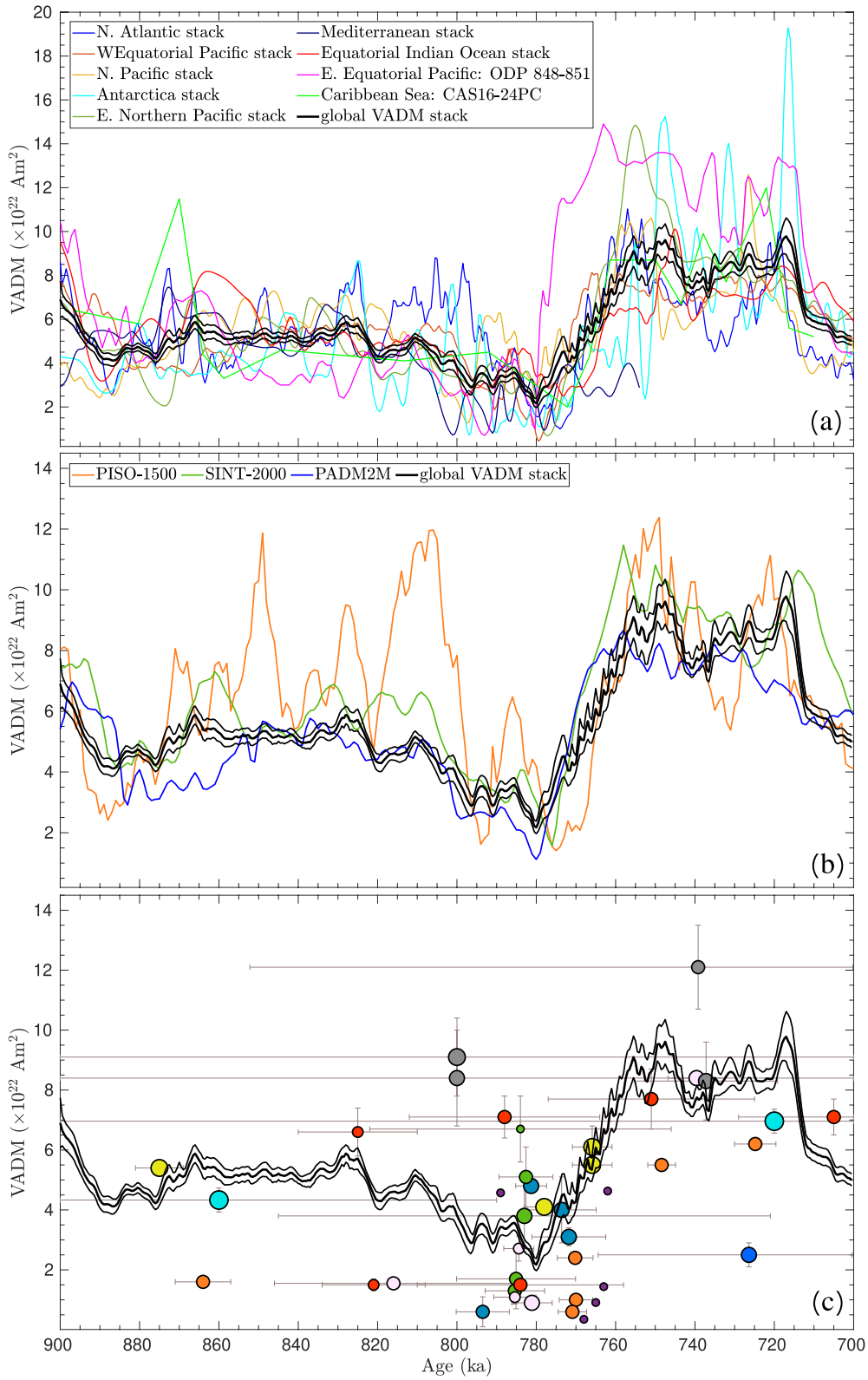

Figure 5. (a) Seven regional virtual axial dipole moment (VADM) stacks, constructed from 35 accepted records by bootstrap resampling, and two individual VADM curves. The global VADM stack (thick black line) with its 95% confidence interval (thin black lines) constructed from these regional stacks is shown. (b) The global VADM stack is compared to previous stacks: SINT-2000 (Valet et al., 2005); PISO-1500 (Channell et al., 2009); and the PADM2M model (Ziegler et al., 2011). (c) Comparison with the volcanic VADM data compiled and evaluated in this study, indicated by the same symbols as in Figure 1.

previous stacks that include the 900–700 ka period, SINT-2000, PSIO-1500, and PADM2M, is given in Figure 5b. The SINT-2000 stack (Valet et al., 2005) was built from 43 records, 33 of which are younger than 800 ka while the remaining 10 are between 2,000 and 800 ka. The PISO-1500 RPI stack (Channell et al., 2009) that covers the past 1,500 ka was created by tandem matching and stacking of 13 paired RPI data and $\delta^{18}O$ records, with a note that most of these records are located in the North Atlantic. PADM2M (Ziegler et al., 2011) is a regularized cubic B-spline VADM model, constructed from global absolute and scaled intensity data. The VADM values in our stack range from ~2 to ~10×10^{22} Am^2, which is comparable to SINT-2000. PADM2M, on the other hand, has relatively lower axial dipole moment strength, which does not exceed ~8×10^{22} Am^2. Between 900 and 780 ka, PISO-1500 has greater amplitudes than our stack, but after 780 ka, they are comparable. We note that our global stack is substantially more consistent to SINT-2000 and PADM2M, while the peaks between 860 and 800 ka in PISO-1500 are similar to intensity maxima found when stacking the individual records dominated by Atlantic data (Figure S6 in Supporting Information S1). The main VADM decrease that occurred at 780 ka in our stack is also seen in PADM2M at the same time, while SINT-2000 and PISO-1500 show the main drop about 5 Kyr later (at 775 ka). The previous stacks drop to a minimum value of ~1×10^{22} Am^2, which is half of the value observed in our stack. Hence, either the scaling of our RPI is systematically too high, or, more likely, our global VADM stack contains non-dipole field contributions, which cannot cancel during the transition as intensity or VADM are always positive values regardless of field polarity. Note that the global, pure axial dipole moment has to be zero at some point in time during the MBR.

When the global VADM stack is compared to the absolute PI-derived VADM data of the 42 lava sites (Figure 5c), reasonable consistency is observed for most regions, considering the uncertainties in age data, PI results, and in the stack itself. Several data from Tahiti, Guadeloupe, Chile, the Canary Islands, Azores Islands, and NW-USA match the stack at 875 ka, ~790–770 ka, and 750–700 ka. The low VADM values obtained at two sites from Canary Islands and Chile in ~820 ka correspond to the global VADM drop indicated in the global VADM stack. Because absolute PI data are more reliable than relative intensities, this consistency demonstrates that the conversion of RPI to absolute intensity was done with a suitable scaling factor.

VADM values for some data are higher than the stack values. Three Mexican VADM data, for instance, are much higher than stack values at 800 ka and 740 ka, and the intensity at one site in Guadeloupe and one site on the Canary Islands are higher than the stack value at 785 ka. However, when the age inaccuracy is considered, the aforementioned disparities are mostly insignificant. Five sites from Hawaii and the Azores exhibit very low VADM values (0.4–1.4 × 10^{22} Am^2) between 770 and 760 ka, which are not reached by our stacked curve nor in previous stacks. In addition, VADM values in two Hawaiian sites with ages 725 and 748 ka are statistically lower than the stack's values. In this comparison we have to keep in mind that each individual VADM value translates non-dipole field contributions to axial dipole moment, which might account for some of the observed discrepancies.

3.2. VGP Latitude Stack

Although directional field variations are expected to differ even more strongly regionally than VADMs, and this is particularly true when the dipole dominance is weak (M. C. Brown et al., 2018; Korte et al., 2019), we construct regional and global VGP stacks to characterize the global field direction change during the MBR. As in VADM, the VGP data of individual records were not temporally aligned and six regional stacks were created by bootstrap resampling. Two individual records (Russian Arctic and Caribbean Sea) were maintained as representative records for the region, as shown in Figure 6a. A global VGP stack was created from these stacks and example curves (Figure 6). As in VADM, a global VGP stack built from all individual records rather than the regional stacks is similar to the North Atlantic regional stack (see Figure S6 in Supporting Information S1) and is not considered here.

All curves indicate reverse polarity directions from 900 to 835 ka (Figure 6a). The North Atlantic curve does not reach as high southern VGP latitudes as the other ones. This observation can be linked to the SR and *T*s of regional data. Records with a high SR and a low *T*s (as in the case of the North Atlantic) should have large amplitudes of directional changes, whereas records with a low SR and a high *T*s should have smooth directional variations. Moreover, as seen in Figure 2b, the North Atlantic region has the most input data. Looking at the VGP distributions of the various regions (Figure S7 in Supporting Information S1) we see that records with the most data points and a high SR have the widest range of VGP latitudes, including rather low values. Sediment cores with high sedimentation rates more likely record short-lived directional anomalies, for example, excursions,

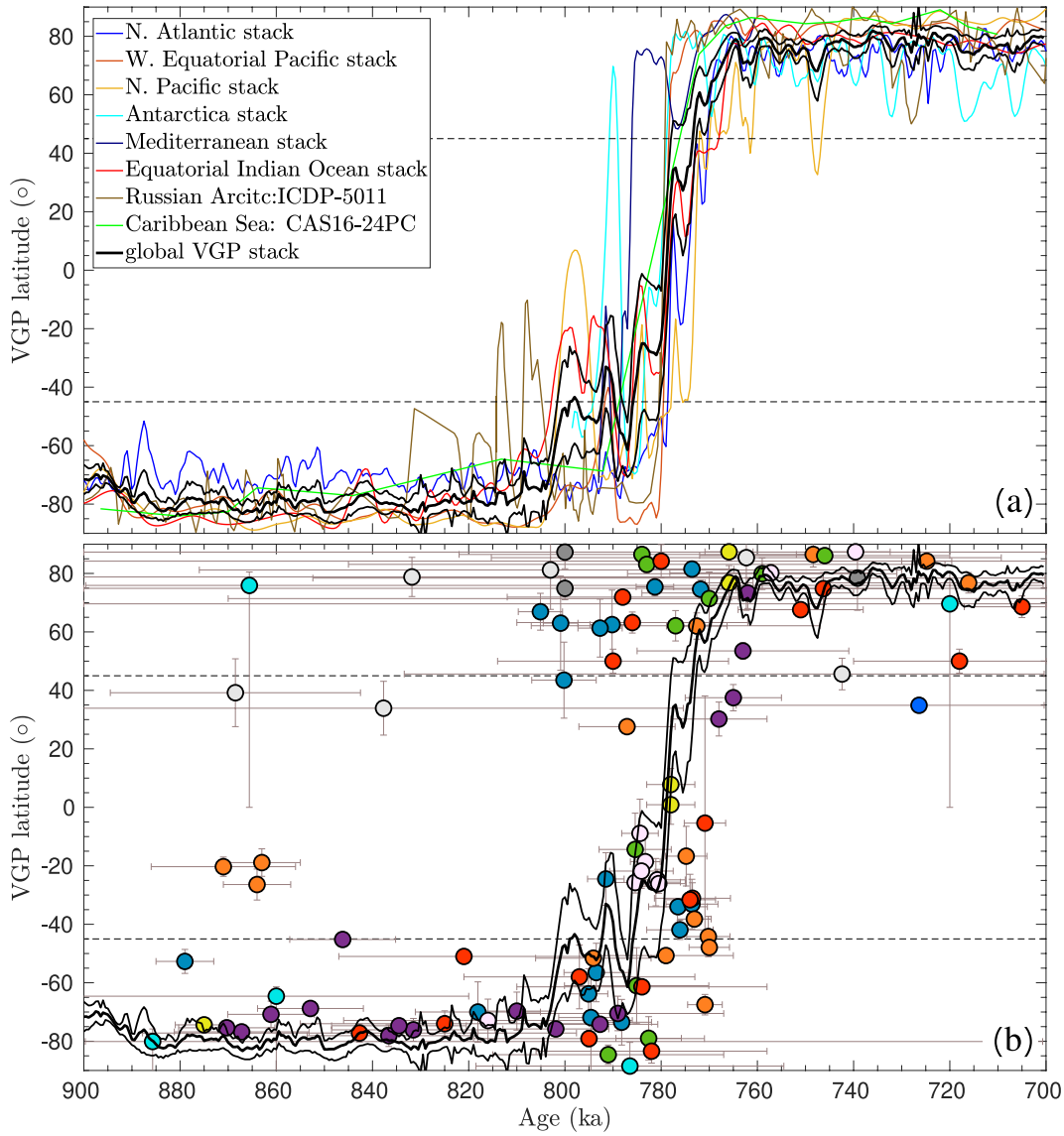

Figure 6. (a) Six regional virtual geomagnetic pole latitude (VGP) stacks constructed from 23 high-quality sediment records, and two representative records of VGP latitude for the Russian Arctic and Caribbean Sea regions. The global VGP stack obtained from them and its 95% confidence interval is shown. (b) Comparison of the global VGP stack with 107 site-mean VGPs calculated from lavas. The two black dashed lines in c indicate VGP latitude ±45°. The symbols for the volcanic regions are the same as in Figure 1.

so their VGPs are more dispersed. Therefore, this regional difference in the VGP latitudes likely does not have magnetic origin. All regions indicate that a sequence of transitional field states developed after 835 ka and lasted until ~770 ka, when the polarity state turned to normal. Unstable field behavior is first observed in the Russian Arctic curve between 831 and 804 ka. However, more records from this region are needed to corroborate this result, which is based on only one record. Then, at ~803–795 ka and ~785 ka, the North Pacific (lat ~ 36°N) and Equatorial Indian Ocean (lat ~ 0°N) stacks show intermediate directions. Also, at ~795 ka, the Antarctic (lat ~ 65°S) and Caribbean sea (lat ~ 15°N) regions both have transitional values. The polarity transition itself then occurred at ~785–768 ka, and it is also recorded sequentially. We find the polarity change first at ~786 ka in the Mediterranean region. At ~785–780 ka, regions from the Western Equatorial Pacific, Equatorial Indian Ocean, Antarctica, and the Russian Arctic all show polarity change. At ~770 ka, the field reverses in the North Atlantic and North Pacific, and finally it is seen in the Equatorial Indian Ocean region at 768 ka. After 768 ka, the different regions show no evidence of a transitional field state. The global VGP stack (Figures 6a and 6b) exhibits the majority of the previously mentioned characteristics. The field polarity was reverse between 900

and ~800 ka, followed by a transitional state between 800 and 773 ka, when the field became normal polarity. The VGP latitudes obtained from 107 lava sites are also shown (Figure 6b). In general, there is good agreement, particularly between the transitional direction seen in the stack at ~784–778 ka and the low VGP latitude values seen in Guadeloupe, Chile, and NW-USA. Low VGP latitude values from Tahiti and Hawaii accompanied the transitional stage noted at 795 ka and 785 ka in the global stack (Figure 6b). The two stable polarity epochs in the stack in general agree well with the lava VGPs. However, some differences between the stack and the lava data exist. For example, between 870 and 770 ka, the normal polarity directions seen at Tahiti, Guadeloupe, the Canary Islands, Iceland, Mexico, and Antarctica differ from the reverse polarity direction obtained from the stack. Between 795 and 780 ka, four regions of lavas (Tahiti, Guadeloupe, Canary, and Azores Islands) have reversed directions, whereas the stack shows transitional polarities. The lava VGP data also reveal a transitional polarity state around ~775–770 ka, where the stack has reached stable polarity. Most of the disparities are small when the age uncertainties are taken into account. Moreover, like VADMs, individual VGPs contain non-dipole field contributions and represent the local directions rather than a global field property. The field in the diverging regions could deviate particularly strongly from the global average, which should be given by the stack, but also might be somewhat biased.

3.3. Paleosecular Variation Index

We use the paleosecular variation index (P_i) suggested by Panovska and Constable (2017) to investigate periods of unstable field during the past 900–700 ka quantitatively. This index measures the departure of the VGP latitude and virtual dipole moment (VDM) from the geographic pole and the present day dipole moment strength, respectively, that is, takes both field direction and intensity information into account to characterize field complexity and variability. Low index values represent a stable, strong, dipole-dominated magnetic field, while high index values characterize unstable and weak magnetic field. To appropriately quantify a threshold value dividing stable from unstable field states, Panovska and Constable (2017) tested this index on recent field models and paleomagnetic data and suggested a threshold of 0.5 for transitional events.

We calculated P_i on local, regional and global scales. The time series of three P_i curves calculated from three sediment records are illustrated in Figure 7a, as examples from which the temporal evolution of the local magnetic field state can be investigated. P_i curves of all records with accepted RPI and directional results are shown in Supporting Information S1 (Figure S8). Most of the analyzed records show transitional field state ($P_i \geq 0.5$) at more than one period. For instance, the P_i curve of site ODP 983 from the North Atlantic shows unstable magnetic field behavior at 859–855 ka, 853–850 ka, and 776–766 ka (Figure 7a). Similarly, record MD90-961 from the Equatorial Indian Ocean shows transitional states at 800–793 ka and 779–771 ka. Moreover, the North Pacific record SO202-1 has transitional states at 900–893 ka and 800–796 ka. From 800 to 796 ka, $P_i \geq 0.5$ was noted in only three data points, with a high value at 796 ka. The large smoothing time of ~8 ka of this record (Section 2.2.3) should be noted. Bootstrap resampling is performed on P_i values of individual records to construct regional P_i stacks using the same methodology as for the VADM and VGP stacks. However, doing so results in unrealistic fits for the North Pacific region, which is caused by one very high P_i value observed in record SO202-1 (Figure 7a). In order to obtain a more realistic regional P_i stack for the North Pacific region, we consider only smoothing spline fits with positive P_i values, and apply this procedure to all regions. We note that it is also possible to use VGP (Figure 6b) and VDM stacks to calculate regional P_i stacks, which gives comparable results (see Figure S9 in Supporting Information S1). Except for the Caribbean Sea, all of the analyzed regions show high P_i values between 800 and 775 ka that reflects the global transitional field state. The lack of transitional field in record CAS16-24PC (see Figures S8 and S9 in Supporting Information S1) could be due to its low SR (1.7 cm/Kyr), which makes it difficult to record quick field changes. The transitional state is first seen in the Equatorial Indian Ocean, Western Equatorial Pacific, North Pacific, and Antarctic regions at ~803–795 ka. Five regions (North Atlantic, Western Equatorial Pacific, Antarctica, Mediterranean, Equatorial Indian Ocean) then have $P_i \geq 0.5$ at 795–790 ka. Between 785 and 770 ka, transitional field states are found almost simultaneously in six regions (except for the Caribbean Sea) which, as will be discussed below, reflects the main phase of the MBR. Our results suggest that the field in the Mediterranean region has transitional behavior between 792 and 781 ka, which is longer than the duration documented in different individual places in this region (Just et al., 2019; Macrì et al., 2018; Sagnotti et al., 2014). We note here the Maffei et al. (2021) deduction that the extreme variations recorded in the Sulmona site (Sagnotti et al., 2014) are spatially localized and only represent a transient feature during a longer transition.

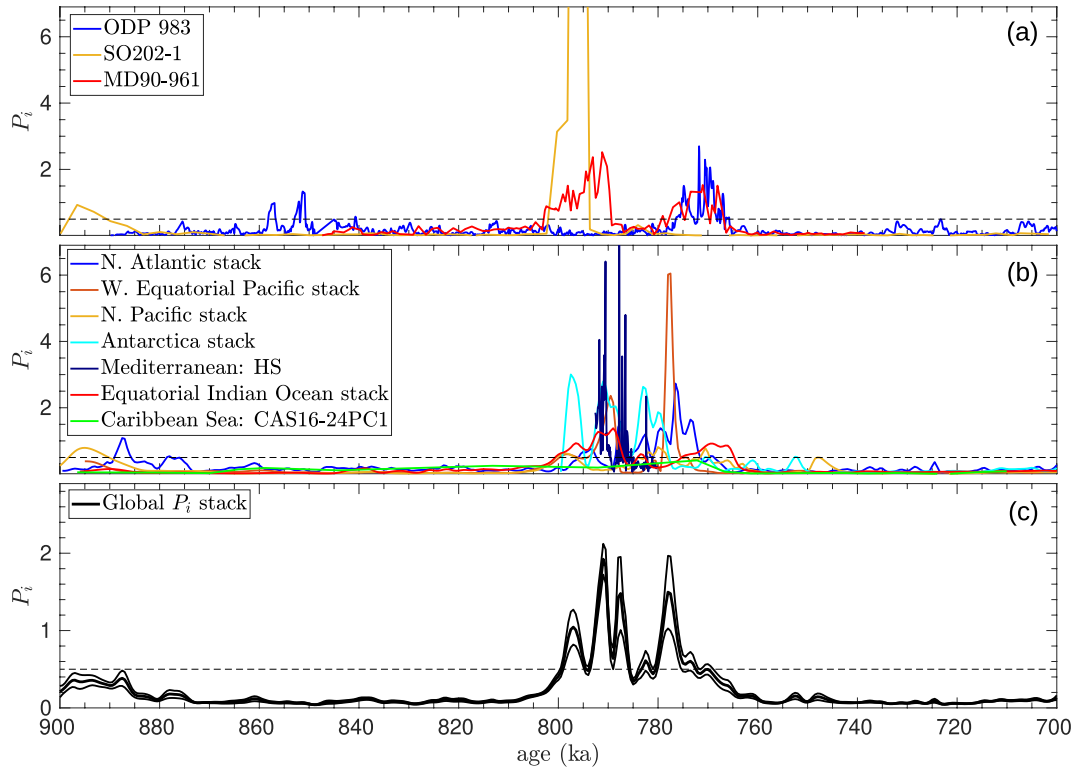

Figure 7. (a) Examples of three paleosecular variation index (P_i) curves established for three individual records accepted in this study. (b) Regional P_i stacks for five regions (N. Atlantic, W. Equatorial Pacific, N. Pacific, Antarctica, and E. Indian Ocean) and two P_i curves (Mediterranean and Caribbean Sea) from one individual record each. (c) Global P_i stack constructed from the seven curves shown in (b). The dashed black horizontal line is the threshold value of 0.5 for P_i, above which transitional field state is proposed. The timing and duration of the Matuyama-Brunhes reversal is calculated, from P_i stack results, to have lasted 30 ka from 800 to 770 ka.

4. Temporal Characteristics of the MBR

4.1. Timing and Duration

A global P_i stack was established (Figure 7c) from the five regional P_i stacks and two P_i curves (Figure 7b). We propose that the time and duration of the MBR can best be estimated using this stack because it considers the full-vector magnetic field information from 18 globally distributed, high-quality sediment records. The field polarity was stable reverse between 900 and 801 ka, followed by a transitional state between 800 and 770 ka, when four intervals of strong field instability occurred, indicated by four P_i peaks. The first three peaks are observed in the interval 800–785 ka, and they are characterized by small drops in the axial dipole moment (Figure 5c) and transitional VGP latitudes (Figure 6b) in some regions, but the field resumed its previous orientation. These short intervals of magnetic field instability can be considered as precursors (Hartl & Tauxe, 1996; Kent & Schneider, 1995; Valet et al., 2012), which are seen regionally, similar to some excursions (see, e.g., Panovska et al., 2019). Although we cannot fully rule out some distortion from age uncertainties in individual records, that facts that the peaks are found in different regional stacks coming from independently dated records and occur at times of moderately low VADM (Figure 5) supports our interpretation. The fourth major phase, which lasts between 780 and 770 ka, is the main polarity transition period, after which the polarity quickly becomes stable in the present day direction. Considering all four peaks, we deduce that the MBR evolved over ~30 Kyr (800–770 ka). We do not find indications for a rebound state (Valet et al., 2012) with our data selection, which is in agreement with the results by Singer et al. (2019).

From the above, the end stage of the Matuyama-Brunhes polarity reversal is around 770 ka. This estimate is consistent with previous findings (Channell et al., 2020; Jouzel et al., 2007; Raisbeck et al., 2006; Singer et al., 2019; Valet et al., 2014) where the mid-point age of the MBR was determined at 773 ka. We find an even longer duration than Singer et al. (2019), who suggested that the MBR evolved over ~22 ka, from 795 to 773 ka,

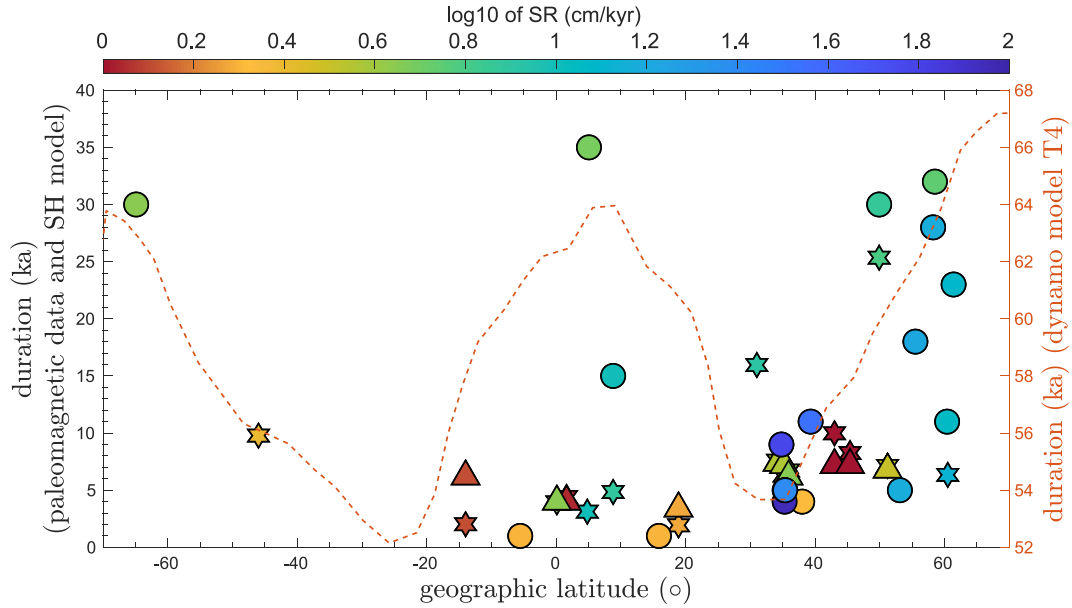

Figure 8. Local Matuyama-Brunhes reversal (MBR) duration plotted against geographic latitude. Local durations of this study (shown in circles) are calculated for 18 records by taking the full field vector into account by use of the paleosecular variation index (P_i). Note that durations calculated for two N. Pacific records (lat. 35.30°N, long. 140.14°E) are identical (each have duration of 5 ka). The durations in Clement (2004) (shown on stars) were estimated from directions only. Duration derived from the spherical harmonic MBR model of Leonhardt and Fabian (2007), on same sites of Clement (2004), is also demonstrated in triangles (all on the left axis). Also shown is the duration estimated from numerical simulation model T4 of Wicht et al. (2009) (dotted brown curve; right axis). Sedimentation rate are shown on a logarithmic color scale to see if they have effect on the estimated duration.

with main instabilities in three successive periods around ~795, ~784, and 773 ka. This is probably due to the substantially lower number of data used by Singer et al. (2019). The inferred duration is much longer than the range of 1–10 ka observed regionally in the IMMAB4 geomagnetic field model (Leonhardt & Fabian, 2007), which spans the interval 795–764 ka. The discrepancy can probably be attributed to IMMAB4's limited data set, which included only three sediment records (609B, 664d, and V16-58) and one volcanic region (La Palma). Actually, these three sediment records are purely POL dated, which aligns the MBR signal, and they were not accepted in our study.

4.2. Relation Between Local Duration and Latitude

The local MBR duration of 18 individual records, defined from P_i curves (Figure S8 in Supporting Information S1), is displayed versus geographic latitude to see if the duration computed in this study depends on latitude. A latitudinal dependence of duration had been suggested by Clement (2004) on four field reversals, including the MBR which was studied in 20 records. Clement (2004) found that the duration increased with latitude, ranging from 2 Kyr at low latitude sites to 12 Kyr at latitudes 50–60° north and south. The duration in Clement (2004) was calculated using only directional data, by estimating the thickness of the stratigraphic section where the polarity switch was observed.

Using the same methodology, Leonhardt and Fabian (2007) evaluated the duration for identical locations (as in Clement (2004)) as predicted from their global IMMAB4 model. The duration estimated from the model is broadly similar with the duration derived from paleomagnetic data, confirming the suggestion made by Clement (2004). Latitudinal dependence of duration has also been found in the numerical dynamo model T4 of Wicht et al. (2009). In order to compare the durations from our full-vector field information with previous values, all these different estimates are plotted in Figure 8. To distinguish between excursions and reversals, Wicht et al. (2009) stipulated that field reversals be separated by a stable period of duration T_s that does not include any excursion. They used three values of T_s to investigate the latitudinal dependence of duration; we include the duration obtained from T_s = 10 Kyr in Figure 8 because it is closest to the durations determined from paleomagnetic data. As seen there,

the durations generated by the numerical model are longer at higher latitudes and at the equator, and shorter at mid-latitude regions.

We first remark that the duration range that we find is different, with durations ranging from 1 to 35 Kyr in our study, which is roughly three times longer than the 2–10 Kyr durations of Clement (2004) and Leonhardt and Fabian (2007). The dynamo model-derived durations (Wicht et al., 2009), on the other hand, are around two times longer than ours and seven times longer than the Clement (2004) and Leonhardt and Fabian (2007) estimates. Note that in Figure 8, we have plotted the paleomagnetic sites used in this study and Clement (2004) and the duration derived from IMMAB4 model (Leonhardt & Fabian, 2007) scaled by SR to see if it has an effect on the calculated durations. We observe short and long durations with distinct SR in our data set, indicating no SR affect. The MBR durations of our high-latitude records (North Atlantic and Antarctica) are generally longer than those of low- to middle-latitude records (Western Equatorial Pacific, Equatorial Indian Ocean, North Pacific, and Mediterranean regions). The same applies to durations of Clement (2004) and Leonhardt and Fabian (2007). This indicates that duration increases with latitude, regardless of how it was calculated. Also, we note that one record from the Equatorial Indian Ocean (lat ∼ 5°N) has a duration of 35 Kyr, while another from the Western Equatorial Pacific (lat ∼ 9°N) has a local duration of 15 Kyr. These durations are longer than those reported in six mid-latitude records (lat ∼35–39°N), suggesting that low- and mid-latitude regions might have different durations. Indeed, this result is similar to the numerical model-derived curve (Figure 8). This observation was believed to be an evidence of the presence of low-latitude reversed flux (Amit et al., 2010; Wicht, 2005; Wicht et al., 2009). However, as we also have two records of latitudes ∼16°N and ∼6°S with durations around one Kyr each, this hypothesis requires further paleomagnetic data to be confirmed. We also notice that two North Atlantic records give durations of ∼5 Kyr and ∼11 Kyr, which are comparable to low and mid-latitude results. More data, in particular from the southern hemisphere, are still needed to fully investigate any latitudinal dependence of MBR duration.

5. Conclusions

High quality paleomagnetic sediment records have been used to produce regional and global stacks of VADM, VGP latitude, and of the paleosecular variation index (P_i) for the past 900–700 ka, that is, the time interval around the Matuyama-Brunhes geomagnetic field reversal. Only well-dated records that have reasonable consistency with surrounding records (if any exist) and that also have no aberrant relative intensity values were accepted. As a result, only 38 sediment records were chosen from a total of 68. The accepted records have a reasonable spatial distribution, though the southern hemisphere is underrepresented, and there are only few records from mid-latitude regions. We calculated the MBR's timing and duration, and investigated the relationship between the local reversal duration and geographic latitude. Unlike previous approaches, we analyze these features by evaluating the full vector field data of the accepted records by use of the P_i, which is computed from both field intensity and direction. At 800 ka, the magnetic field became unstable, indicating the start of the MBR, which ended at 770 ka. It has been shown, from regional and global VADM stacks, that the global axial dipole moment began to steadily drop ∼10 Kyr before the onset of the reversal. The 770 ka age for the end of the polarity reversal at a global scale determined in this work corresponds well with the mid-point age (773 ka) reported previously from high-quality and high SR marine cores. The ∼30-kyr MBR duration is even longer than the 22-kyr evolution time proposed recently based on a compilation of well-dated lava flows, sediments, and ice cores, according to which the MBR evolved between 795 and 773 ka. Our estimate's longer duration may be explained by the fact that it is based on a larger data set. The prior idea that local reversal duration is latitudinal dependent is generally confirmed in this study, as high-latitude records from the north and south hemisphere have longer durations than those found at low-to-medium latitudes. We also found indications for longer duration at very low latitudes similar to earlier results from a numerical dynamo simulation, but these results might not be robust as nearby records suggest short duration. More data from a wider range of locations is still required to establish the relation between MBR duration and latitude. The new data compilation presented here will be used to build a new global SH model of the Matuyama-Brunhes reversal.

Data Availability Statement

Data of regional and global stacks of the virtual dipole moment, virtual geomagnetic pole latitude, and paleosecular variation index, which were calculated in this study, as well as the paleomagnetic data of accepted sediment records compiled from previous studies can be found at https://earthref.org/ERDA/2545/.

Acknowledgments
The Alexander von Humboldt Foundation awarded A.N. Mahgoub a research fellowship, which he expressed thanks for. S. Panovska gratefully acknowledges the Discovery Fellowship at the GFZ Potsdam, Germany. We would like to express a deep appreciation to all authors who shared their data with us personally, or made the data available through supporting information and public databases. We also thank Leonardo Sagnotti and an anonymous reviewer for their constructive comments and suggestions. Open Access funding enabled and organized by Projekt DEAL.

References

Abdel-Monem, A., Watkins, N., & Gast, P. (1972). Potassium-argon ages, volcanic stratigraphy, and geomagnetic polarity history of the Canary Islands; Tenerife, La Palma and Hierro. *American Journal of Science*, *272*(9), 805–825. https://doi.org/10.2475/ajs.272.9.805

Ahn, S., Khider, D., Lisiecki, L. E., & Lawrence, C. E. (2017). A probabilistic Pliocene–Pleistocene stack of benthic δ^{18}O using a profile hidden Markov model. *Dynamics and Statistics of the Climate System*, *2*(1), dzx002. https://doi.org/10.1093/climsys/dzx002

Aitken, M., Allsop, A., Bussell, G., & Winter, M. (1988). Determination of the intensity of the Earth's magnetic field during archaeological times: Reliability of the Thellier technique. *Reviews of Geophysics*, *26*(1), 3–12. https://doi.org/10.1029/rg026i001p00003

Alken, P., Thébault, E., Beggan, C. D., Amit, H., Aubert, J., Baerenzung, J., et al. (2021). International geomagnetic reference field: The thirteenth generation. *Earth Planets and Space*, *73*(1), 1–25.

Alva-Valdivia, L. M., Goguitchaichvili, A., & Urrutia-Fucugauchi, J. (2001). Further constraints for the Plio-Pleistocene geomagnetic field strength. *Earth Planets and Space*, *53*(9), 873–881. https://doi.org/10.1186/bf03351684

Amit, H., Leonhardt, R., & Wicht, J. (2010). Polarity reversals from paleomagnetic observations and numerical dynamo simulations. *Space Science Reviews*, *155*(1), 293–335. https://doi.org/10.1007/s11214-010-9695-2

Arason, P., & Levi, S. (1990). Compaction and inclination shallowing in deep-sea sediments from the Pacific Ocean. *Journal of Geophysical Research*, *95*(B4), 4501–4510. https://doi.org/10.1029/jb095ib04p04501

Armstrong, R. L. (1978). K-Ar dating: Late Cenozoic McMurdo volcanic group and dry valley glacial history, Victoria Land, Antarctica. *New Zealand Journal of Geology and Geophysics*, *21*(6), 685–698. https://doi.org/10.1080/00288306.1978.10425199

Baksi, A., Hsu, V., McWilliams, M., & Farrar, E. (1992). ^{40}Ar/^{39}Ar dating of the Brunhes-Matuyama geomagnetic field reversal. *Science*, *256*(5055), 356–357. https://doi.org/10.1126/science.256.5055.356

Balbas, A. M., Koppers, A. A., Clark, P. U., Coe, R. S., Reilly, B. T., Stoner, J. S., & Konrad, K. (2018). Millennial-Scale instability in the geomagnetic field prior to the Matuyama-Brunhes reversal. *Geochemistry, Geophysics, Geosystems*, *19*(3), 952–967. https://doi.org/10.1002/2017gc007404

Bassinot, F. C., Labeyrie, L. D., Vincent, E., Quidelleur, X., Shackleton, N. J., & Lancelot, Y. (1994). The astronomical theory of climate and the age of the Brunhes-Matuyama magnetic reversal. *Earth and Planetary Science Letters*, *126*(1–3), 91–108. https://doi.org/10.1016/0012-821x(94)90244-5

Bieber, A., St-Onge, G., Feuillet, N., Carlut, J., Moreno, E., & Michel, E. (2021). Regional chronostratigraphy in the eastern Lesser Antilles quaternary fore-arc and accretionary wedge sediments: Relative paleointensity, oxygen isotopes and reversals. *Quaternary Geochronology*, *65*, 101179. https://doi.org/10.1016/j.quageo.2021.101179

Biggin, A. J., & Paterson, G. A. (2014). A new set of qualitative reliability criteria to aid inferences on palaeomagnetic dipole moment variations through geological time. *Frontiers of Earth Science*, *2*, 24. https://doi.org/10.3389/feart.2014.00024

Blanc, F. (1983). Corrélations chronologiques et géochimiques des formations volcaniques du sud de la basse terre de Guadeloupe (petites Antilles): Début du cycle récent (Unpublished doctoral dissertation). Université Scientifique et Médicale de Grenoble.

Bono, R. K., Paterson, G. A., van der Boon, A., Engbers, Y. A., Michael Grappone, J., Handford, B., et al. (2022). The PINT database: A definitive compilation of absolute palaeomagnetic intensity determinations since 4 billion years ago. *Geophysical Journal International*, *229*(1), 522–545. https://doi.org/10.1093/gji/ggab490

Brown, L. L., Singer, B. S., Pickens, J. C., & Jicha, B. R. (2004). Paleomagnetic directions and ^{40}Ar/^{39}Ar ages from the Tatara-San Pedro volcanic complex, Chilean Andes: Lava record of a Matuyama-Brunhes precursor? *Journal of Geophysical Research*, *109*(B12), B12101. https://doi.org/10.1029/2004jb003007

Brown, M. C., Gratton, M. N., Shaw, J., Holme, R., & Soler, V. (2009). Microwave palaeointensity results from the Matuyama–Brunhes geomagnetic field reversal. *Physics of the Earth and Planetary Interiors*, *173*(1–2), 75–102. https://doi.org/10.1016/j.pepi.2008.11.001

Brown, M. C., Jicha, B., Singer, B. S., & Shaw, J. (2013). Snapshot of the Matuyama-Brunhes reversal process recorded in ^{40}Ar/^{39}Ar-dated lavas from Guadeloupe, West Indies. *Geochemistry, Geophysics, Geosystems*, *14*(10), 4341–4350. https://doi.org/10.1002/ggge.20263

Brown, M. C., Korte, M., Holme, R., Wardinski, I., & Gunnarson, S. (2018). Earth's magnetic field is probably not reversing. *Proceedings of the National Academy of Sciences of the United States of America*, *115*(20), 5111–5116. https://doi.org/10.1073/pnas.1722110115

Butler, R. F. (1992). *Paleomagnetism: Magnetic domains to geologic terranes* (Vol. 319). Blackwell Scientific Publications.

Camps, P., Singer, B., Carvallo, C., Goguitchaichvili, A., Fanjat, G., & Allen, B. (2011). The Kamikatsura event and the Matuyama–Brunhes reversal recorded in lavas from Tjörnes Peninsula, northern Iceland. *Earth and Planetary Science Letters*, *310*(1–2), 33–44. https://doi.org/10.1016/j.epsl.2011.07.026

Cande, S. C., & Kent, D. V. (1995). Revised calibration of the geomagnetic polarity timescale for the late Cretaceous and Cenozoic. *Journal of Geophysical Research*, *100*(B4), 6093–6095. https://doi.org/10.1029/94jb03098

Carcaillet, J. T., Thouveny, N., & Bourles, D. L. (2003). Geomagnetic moment instability between 0.6 and 1.3 Ma from cosmonuclide evidence. *Geophysical Research Letters*, *30*(15), 1792. https://doi.org/10.1029/2003gl017550

Carlut, J., Quidelleur, X., Courtillot, V., & Boudon, G. (2000). Paleomagnetic directions and K/Ar dating of 0 to 1 Ma lava flows from La Guadeloupe Island (French West Indies): Implications for time-averaged field models. *Journal of Geophysical Research*, *105*(B1), 835–849. https://doi.org/10.1029/1999jb900238

Channell, J. (2017). Complexity in Matuyama–Brunhes polarity transitions from North Atlantic IODP/ODP deep-sea sites. *Earth and Planetary Science Letters*, *467*, 43–56. https://doi.org/10.1016/j.epsl.2017.03.019

Channell, J., Curtis, J., & Flower, B. (2004). The Matuyama-Brunhes boundary interval (500-900 ka) in North Atlantic drift sediments. *Geophysical Journal International*, *158*(2), 489–505. https://doi.org/10.1111/j.1365-246x.2004.02329.x

Channell, J., Hodell, D., McManus, J., & Lehman, B. (1998). Orbital modulation of the Earth's magnetic field intensity. *Nature*, *394*(6692), 464–468. https://doi.org/10.1038/28833

Channell, J., Hodell, D., Xuan, C., Mazaud, A., & Stoner, J. (2008). Age calibrated relative paleointensity for the last 1.5 Myr at IODP site U1308 (North Atlantic). *Earth and Planetary Science Letters*, *274*(1–2), 59–71. https://doi.org/10.1016/j.epsl.2008.07.005

Channell, J., Hodell, D. A., Romero, O., Hillaire-Marcel, C., de Vernal, A., Stoner, J. S., et al. (2012). A 750-kyr detrital-layer stratigraphy for the North Atlantic (IODP sites U1302–U1303, Orphan Knoll, Labrador Sea). *Earth and Planetary Science Letters*, *317*, 218–230. https://doi.org/10.1016/j.epsl.2011.11.029

Channell, J., Hodell, D. A., Singer, B., & Xuan, C. (2010). Reconciling astrochronological and ^{40}Ar/^{39}Ar ages for the Matuyama-Brunhes boundary and late Matuyama Chron. *Geochemistry, Geophysics, Geosystems*, *11*(12), Q0AA12. https://doi.org/10.1029/2010gc003203

Channell, J., & Kleiven, H. (2000). Geomagnetic palaeointensities and astrochronological ages for the Matuyama–Brunhes boundary and the boundaries of the Jaramillo subchron: Palaeomagnetic and oxygen isotope records from ODP site 983. *Philosophical Transactions of the Royal Society of London. Series A: Mathematical, Physical and Engineering Sciences*, *358*(1768), 1027–1047. https://doi.org/10.1098/rsta.2000.0572

Channell, J., & Raymo, M. (2003). Paleomagnetic record at ODP site 980 (Feni drift, Rockall) for the past 1.2 Myrs. *Geochemistry, Geophysics, Geosystems*, *4*(4), 1033. https://doi.org/10.1029/2002gc000440

Channell, J., Singer, B., & Jicha, B. R. (2020). Timing of Quaternary geomagnetic reversals and excursions in volcanic and sedimentary archives. *Quaternary Science Reviews*, *228*, 106114. https://doi.org/10.1016/j.quascirev.2019.106114

Channell, J., Wright, J., Mazaud, A., & Stoner, J. (2014). Age through tandem correlation of Quaternary relative paleointensity (RPI) and oxygen isotope data at IODP Site U1306 (Eirik Drift, SW Greenland). *Quaternary Science Reviews*, *88*, 135–146. https://doi.org/10.1016/j.quascirev.2014.01.022

Channell, J., Xuan, C., & Hodell, D. (2009). Stacking paleointensity and oxygen isotope data for the last 1.5 Myr (PISO-1500). *Earth and Planetary Science Letters*, *283*(1–4), 14–23. https://doi.org/10.1016/j.epsl.2009.03.012

Chauvin, A., Roperch, P., & Duncan, R. A. (1990). Records of geomagnetic reversals from volcanic islands of French Polynesia: 2. Paleomagnetic study of a flow sequence (1.2–0.6 Ma) from the island of Tahiti and discussion of reversal models. *Journal of Geophysical Research*, *95*(B3), 2727–2752. https://doi.org/10.1029/jb095ib03p02727

Clement, B. M. (1991). Geographical distribution of transitional VGPs: Evidence for non-zonal equatorial symmetry during the Matuyama-Brunhes geomagnetic reversal. *Earth and Planetary Science Letters*, *104*(1), 48–58. https://doi.org/10.1016/0012-821x(91)90236-b

Clement, B. M. (2004). Dependence of the duration of geomagnetic polarity reversals on site latitude. *Nature*, *428*(6983), 637–640. https://doi.org/10.1038/nature02459

Clement, B. M., & Kent, D. V. (1984). Latitudinal dependency of geomagnetic polarity transition durations. *Nature*, *310*(5977), 488–491. https://doi.org/10.1038/310488a0

Clement, B. M., & Kent, D. V. (1987). Short polarity intervals within the Matuyama: Transitional field records from hydraulic piston cored sediments from the North Atlantic. *Earth and Planetary Science Letters*, *81*(2–3), 253–264. https://doi.org/10.1016/0012-821x(87)90161-0

Clement, B. M., & Kent, D. V. (1991). A southern hemisphere record of the Matuyama-Brunhes polarity reversal. *Geophysical Research Letters*, *18*(1), 81–84. https://doi.org/10.1029/90gl02714

Coe, R. S. (1967). Paleo-intensities of the Earth's magnetic field determined from Tertiary and Quaternary rocks. *Journal of Geophysical Research*, *72*(12), 3247–3262. https://doi.org/10.1029/jz072i012p03247

Coe, R. S., Singer, B., Pringle, M. S., & Zhao, X. (2004). Matuyama–Brunhes reversal and Kamikatsura event on Maui: Paleomagnetic directions, $^{40}Ar/^{39}Ar$ ages and implications. *Earth and Planetary Science Letters*, *222*(2), 667–684. https://doi.org/10.1016/j.epsl.2004.03.003

Cohen, K. M., & Gibbard, P. (2019). Global chronostratigraphical correlation table for the last 2.7 million years, version 2019 QI-500. *Quaternary International*, *500*, 20–31. https://doi.org/10.1016/j.quaint.2019.03.009

Deamer, G. A., & Kodama, K. P. (1990). Compaction-induced inclination shallowing in synthetic and natural clay-rich sediments. *Journal of Geophysical Research*, *95*(B4), 4511–4529. https://doi.org/10.1029/jb095ib04p04511

Dekkers, M. J., & Böhnel, H. N. (2006). Reliable absolute palaeointensities independent of magnetic domain state. *Earth and Planetary Science Letters*, *248*(1–2), 508–517. https://doi.org/10.1016/j.epsl.2006.05.040

Dinarès-Turell, J., Sagnotti, L., & Roberts, A. P. (2002). Relative geomagnetic paleointensity from the Jaramillo subchron to the Matuyama/Brunhes boundary as recorded in a Mediterranean piston core. *Earth and Planetary Science Letters*, *194*(3–4), 327–341. https://doi.org/10.1016/s0012-821x(01)00563-5

Evans, M., & Muxworthy, A. (2018). A re-appraisal of the proposed rapid Matuyama–Brunhes geomagnetic reversal in the Sulmona Basin. Italy. *Geophysical Journal International*, *213*(3), 1744–1750. https://doi.org/10.1093/gji/ggy111

Fleck, R. J., Hagstrum, J. T., Calvert, A. T., Evarts, R. C., & Conrey, R. M. (2014). $^{40}Ar/^{39}Ar$ geochronology, paleomagnetism, and evolution of the Boring volcanic field, Oregon and Washington, USA. *Geosphere*, *10*(6), 1283–1314. https://doi.org/10.1130/ges00985.1

Gillot, P.-Y., & Cornette, Y. (1986). The cassignol technique for potassium—Argon dating, precision and accuracy: Examples from the late pleistocene to recent volcanics from southern Italy. *Chemical Geology: Isotope Geoscience section*, *59*, 205–222. https://doi.org/10.1016/0168-9622(86)90072-2

Gradstein, F. M., Ogg, J. G., Schmitz, M. D., & Ogg, G. M. (2012). *The geologic time scale 2012*. Elsevier.

Gratton, M. N., Shaw, J., & Brown, L. L. (2007). Absolute palaeointensity variation during a precursor to the Matuyama-Brunhes transition recorded in Chilean lavas. *Physics of the Earth and Planetary Interiors*, *162*(1–2), 61–72. https://doi.org/10.1016/j.pepi.2007.03.003

Guillou, H., Carracedo, J. C., Torrado, F. P., & Badiola, E. R. (1996). K-Ar ages and magnetic stratigraphy of a hotspot-induced, fast grown oceanic island: El Hierro, Canary Islands. *Journal of Volcanology and Geothermal Research*, *73*(1–2), 141–155. https://doi.org/10.1016/0377-0273(96)00021-2

Guyodo, Y., Acton, G. D., Brachfeld, S., & Channell, J. (2001). A sedimentary paleomagnetic record of the Matuyama chron from the Western Antarctic margin (ODP Site 1101). *Earth and Planetary Science Letters*, *191*(1–2), 61–74. https://doi.org/10.1016/s0012-821x(01)00402-2

Guyodo, Y., & Valet, J.-P. (1999). Global changes in intensity of the Earth's magnetic field during the past 800 Kyr. *Nature*, *399*(6733), 249–252. https://doi.org/10.1038/20420

Hagstrum, J. T., Fleck, R. J., Evarts, R. C., & Calvert, A. T. (2017). Paleomagnetism and $^{40}Ar/^{39}Ar$ geochronology of the Plio-Pleistocene Boring Volcanic Field: Implications for the geomagnetic polarity time scale and paleosecular variation. *Physics of the Earth and Planetary Interiors*, *262*, 101–115. https://doi.org/10.1016/j.pepi.2016.07.008

Haneda, Y., Okada, M., Suganuma, Y., & Kitamura, T. (2020). A full sequence of the Matuyama–Brunhes geomagnetic reversal in the Chiba composite section, Central Japan. *Progress in Earth and Planetary Science*, *7*(1), 1–22. https://doi.org/10.1186/s40645-020-00354-y

Hartl, P., & Tauxe, L. (1996). A precursor to the Matuyama/Brunhes transition-field instability as recorded in pelagic sediments. *Earth and Planetary Science Letters*, *138*(1–4), 121–135. https://doi.org/10.1016/0012-821x(95)00231-z

Hatfield, R., Stoner, J., & Fraass, A. (2021). Relative paleointensity record of integrated ocean drilling program site U1396 in the Caribbean Sea: Geomagnetic and chronostratigraphic observations in the pliocene. *Geochemistry, Geophysics, Geosystems*, *22*(7), e2021GC009677. https://doi.org/10.1029/2021gc009677

Hayashida, A., Verosub, K. L., Heider, F., & Leonhardt, R. (1999). Magnetostratigraphy and relative palaeointensity of late Neogene sediments at ODP Leg 167 site 1010 off Baja California. *Geophysical Journal International*, *139*(3), 829–840. https://doi.org/10.1046/j.1365-246x.1999.00979.x

Hilgen, F. (1991). Astronomical calibration of Gauss to Matuyama sapropels in the Mediterranean and implication for the geomagnetic polarity time scale. *Earth and Planetary Science Letters*, *104*(2–4), 226–244. https://doi.org/10.1016/0012-821x(91)90206-w

Hill, M. J., & Shaw, J. (1999). Palaeointensity results for historic lavas from Mt Etna using microwave demagnetization/remagnetization in a modified Thellier-type experiment. *Geophysical Journal International*, *139*(2), 583–590. https://doi.org/10.1046/j.1365-246x.1999.00980.x

Hoffman, K. A. (2000). Temporal aspects of the last reversal of Earth's magnetic field. *Philosophical Transactions of the Royal Society of London. Series A: Mathematical, Physical and Engineering Sciences*, *358*(1768), 1181–1190. https://doi.org/10.1098/rsta.2000.0580

Hoffman, K. A., & Fuller, M. (1978). Transitional field configurations and geomagnetic reversal. *Nature*, *273*(5665), 715–718. https://doi.org/10.1038/273715a0

Horng, C.-S., Lee, M.-Y., Palike, H., Wei, K.-Y., Liang, W.-T., Iizuka, Y., & Torii, M. (2002). Astronomically calibrated ages for geomagnetic reversals within the Matuyama chron. *Earth Planets and Space*, *54*(6), 679–690. https://doi.org/10.1186/bf03351719

Horng, C.-S., Roberts, A. P., & Liang, W.-T. (2003). A 2.14-Myr astronomically tuned record of relative geomagnetic paleointensity from the western Philippine Sea. *Journal of Geophysical Research*, *108*(B1), 2059. https://doi.org/10.1029/2001jb001698

Huang, Y.-S., Lee, T.-Q., Hsu, S.-K., & Yang, T.-N. (2009). Paleomagnetic field variation with strong negative inclination during the Brunhes chron at the Banda Sea, equatorial southwestern Pacific. *Physics of the Earth and Planetary Interiors*, *173*(1–2), 162–170. https://doi.org/10.1016/j.pepi.2008.11.013

Hyodo, M., Biswas, D. K., Noda, T., Tomioka, N., Mishima, T., Itota, C., & Sato, H. (2006). Millennial-to submillennial-scale features of the Matuyama-Brunhes geomagnetic polarity transition from Osaka Bay, southwestern Japan. *Journal of Geophysical Research*, *111*(B2), B02103. https://doi.org/10.1029/2004jb003584

Hyodo, M., & Kitaba, I. (2015). Timing of the Matuyama–Brunhes geomagnetic reversal: Decoupled thermal maximum and sea-level highstand during marine isotope stage 19. *Quaternary International*, *383*, 136–144. https://doi.org/10.1016/j.quaint.2015.01.052

Imbrie, J., Hays, J. D., Martinson, D. G., McIntyre, A., Mix, A. C., Morley, J. J., et al. (1984). The orbital theory of Pleistocene climate: Support from a revised chronology of the marine δ18O record. In A.L. Berger, J. Imbrie, & J. Hays, (Eds.), *Milankovitch and climate* (Vol. 1, pp. 269–305). D. Reidel Publishing Company.

Ingham, M., & Turner, G. (2008). Behaviour of the geomagnetic field during the Matuyama–Brunhes polarity transition. *Physics of the Earth and Planetary Interiors*, *168*(3–4), 163–178. https://doi.org/10.1016/j.pepi.2008.06.008

Johnson, C. L., Wijbrans, J. R., Constable, C. G., Gee, J., Staudigel, H., Tauxe, L., et al. (1998). $^{40}Ar/^{39}Ar$ ages and paleomagnetism of Sao Miguel lavas, Azores. *Earth and Planetary Science Letters*, *160*(3–4), 637–649. https://doi.org/10.1016/s0012-821x(98)00117-4

Jouzel, J., Masson-Delmotte, V., Cattani, O., Dreyfus, G., Falourd, S., Hoffmann, G., et al. (2007). Orbital and millennial Antarctic climate variability over the past 800,000 years. *Science*, *317*(5839), 793–796. https://doi.org/10.1126/science.1141038

Just, J., Sagnotti, L., Nowaczyk, N. R., Francke, A., & Wagner, B. (2019). Recordings of fast paleomagnetic reversals in a 1.2 Ma greigite-rich sediment archive from Lake Ohrid, Balkans. *Journal of Geophysical Research: Solid Earth*, *124*(12), 12445–12464. https://doi.org/10.1029/2019jb018297

Kent, D. V., & Opdyke, N. D. (1977). Palaeomagnetic field intensity variation recorded in a Brunhes epoch deep-sea sediment core. *Nature*, *266*(5598), 156–159. https://doi.org/10.1038/266156a0

Kent, D. V., & Schneider, D. A. (1995). Correlation of paleointensity variation records in the Brunhes/Matuyama polarity transition interval. *Earth and Planetary Science Letters*, *129*(1–4), 135–144. https://doi.org/10.1016/0012-821x(94)00236-r

Khramov, A. (1987). *Paleomagnetology* (p. 308). Springer-Verlag.

Kok, Y. S., & Tauxe, L. (1999). A relative geomagnetic paleointensity stack from Ontong-Java Plateau sediments for the Matuyama. *Journal of Geophysical Research*, *104*(B11), 25401–25413. https://doi.org/10.1029/1999jb900186

Korff, L., Von Dobeneck, T., Frederichs, T., Kasten, S., Kuhn, G., Gersonde, R., & Diekmann, B. (2016). Cyclic magnetite dissolution in pleistocene sediments of the abyssal northwest Pacific Ocean: Evidence for glacial oxygen depletion and carbon trapping. *Paleoceanography*, *31*(5), 600–624. https://doi.org/10.1002/2015pa002882

Korte, M., Brown, M. C., Panovska, S., & Wardinski, I. (2019). Robust characteristics of the laschamp and Mono lake geomagnetic excursions: Results from global field models. *Frontiers of Earth Science*, *7*, 86. https://doi.org/10.3389/feart.2019.00086

Kuiper, K., Deino, A., Hilgen, F., Krijgsman, W., Renne, P., & Wijbrans, J. (2008). Synchronizing rock clocks of Earth history. *Science*, *320*(5875), 500–504. https://doi.org/10.1126/science.1154339

Laj, C., Kissel, C., & Beer, J. (2004). High resolution global paleointensity stack since 75 kyr (GLOPIS-75) calibrated to absolute values. In J. E. T. Channell, D. V. Kent, W. Lowrie, & J. G. Meert (Eds.), *Timescales Of the paleomagnetic field, Geophysical Monograph Series* (Vol. 145, pp. 255–265). American Geophysical Union. https://doi.org/10.1029/145GM19

Laj, C., Kissel, C., Garnier, F., & Herrero-Bervera, E. (1996). Relative geomagnetic field intensity and reversals for the last 1.8 My from a central equatorial Pacific core. *Geophysical Research Letters*, *23*(23), 3393–3396. https://doi.org/10.1029/96gl03261

Laj, C., Mazaud, A., Weeks, R., Fuller, M., & Herrero-Bervera, E. (1991). Geomagnetic reversal paths. *Nature*, *351*(6326), 447. https://doi.org/10.1038/351447a0

Langereis, C., Van Hoof, A., & Rochette, P. (1992). Longitudinal confinement of geomagnetic reversal paths as a possible sedimentary artefact. *Nature*, *358*(6383), 226–230. https://doi.org/10.1038/358226a0

Lawrence, K., Tauxe, L., Staudigel, H., Constable, C., Koppers, A., McIntosh, W., & Johnson, C. (2009). Paleomagnetic field properties at high southern latitude. *Geochemistry, Geophysics, Geosystems*, *10*(1), Q01005. https://doi.org/10.1029/2008gc002072

Leonhardt, R., & Fabian, K. (2007). Paleomagnetic reconstruction of the global geomagnetic field evolution during the Matuyama/Brunhes transition: Iterative Bayesian inversion and independent verification. *Earth and Planetary Science Letters*, *253*(1–2), 172–195. https://doi.org/10.1016/j.epsl.2006.10.025

Leonhardt, R., Heider, F., & Hayashida, A. (1999). Relative geomagnetic field intensity across the Jaramillo subchron in sediments from the California margin: Ocean drilling program Leg 167. *Journal of Geophysical Research*, *104*(B12), 29133–29146. https://doi.org/10.1029/1999jb900268

Leonhardt, R., McWilliams, M., Heider, F., & Soffel, H. (2009). The Gilsá excursion and the Matuyama/Brunhes transition recorded in $^{40}Ar/^{39}Ar$ dated lavas from Lanai and Maui, Hawaiian Islands. *Geophysical Journal International*, *179*(1), 43–58. https://doi.org/10.1111/j.1365-246x.2009.04264.x

Lhuillier, F., Shcherbakov, V. P., Gilder, S. A., & Hagstrum, J. T. (2017). Variability of the 0–3 Ma palaeomagnetic field observed from the Boring volcanic field of the Pacific northwest. *Geophysical Journal International*, *211*(1), 69–79. https://doi.org/10.1093/gji/ggx288

Lisiecki, L. E., & Raymo, M. E. (2005). A Pliocene-Pleistocene stack of 57 globally distributed benthic $\delta^{18}O$ records. *Paleoceanography*, *20*(1), PA1003. https://doi.org/10.1029/2004pa001071

Love, J., & Mazaud, A. (1997). A database for the Matuyama-Brunhes magnetic reversal. *Physics of the Earth and Planetary Interiors*, *103*(3–4), 207–245. https://doi.org/10.1016/s0031-9201(97)00034-4

Lund, S. P., & Keigwin, L. (1994). Measurement of the degree of smoothing in sediment paleomagnetic secular variation records: An example from late quaternary deep-sea sediments of the Bermuda rise, western North Atlantic Ocean. *Earth and Planetary Science Letters*, *122*(3–4), 317–330. https://doi.org/10.1016/0012-821x(94)90005-1

Macrì, P., Capraro, L., Ferretti, P., & Scarponi, D. (2018). A high-resolution record of the Matuyama-Brunhes transition from the Mediterranean region: The Valle di Manche section (Calabria, Southern Italy). *Physics of the Earth and Planetary Interiors*, *278*, 1–15. https://doi.org/10.1016/j.pepi.2018.02.005

Macrì, P., Sagnotti, L., Dinarès-Turell, J., & Caburlotto, A. (2005). A composite record of Late Pleistocene relative geomagnetic paleointensity from the Wilkes Land Basin (Antarctica). *Physics of the Earth and Planetary Interiors*, *151*(3–4), 223–242. https://doi.org/10.1016/j.pepi.2005.03.004

Macrì, P., Sagnotti, L., Dinarès-Turell, J., & Caburlotto, A. (2010). Relative geomagnetic paleointensity of the Brunhes Chron and the Matuyama–Brunhes precursor as recorded in sediment core from Wilkes Land Basin (Antarctica). *Physics of the Earth and Planetary Interiors*, *179*(1–2), 72–86. https://doi.org/10.1016/j.pepi.2009.12.002

Maegakiuchi, K., Hyodo, M., Kitaba, I., Hirose, K., Katoh, S., & Sato, H. (2016). Brief sea-level fall event and centennial to millennial sea-level variations during Marine Isotope Stage 19 in Osaka Bay, Japan. *Journal of Quaternary Science*, *31*(7), 809–822. https://doi.org/10.1002/jqs.2907

Maffei, S., Livermore, P. W., Mound, J. E., Greenwood, S., & Davies, C. J. (2021). Fast directional changes during geomagnetic transitions: Global reversals or local fluctuations? *Geosciences*, *11*(8), 318. https://doi.org/10.3390/geosciences11080318

Mankinen, E. A., & Dalrymple, G. B. (1979). Revised geomagnetic polarity time scale for the interval 0–5 My BP. *Journal of Geophysical Research*, *84*(B2), 615–626. https://doi.org/10.1029/jb084ib02p00615

Mankinen, E. A., & Wentworth, C. M. (2016). Paleomagnetic record determined in cores from deep research wells in the Quaternary Santa Clara basin, California. *Geosphere*, *12*(1), 35–57. https://doi.org/10.1130/ges01217.1

Mark, D. F., Renne, P. R., Dymock, R. C., Smith, V. C., Simon, J. I., Morgan, L. E., et al. (2017). High-precision $^{40}Ar/^{39}Ar$ dating of Pleistocene tuffs and temporal anchoring of the Matuyama-Brunhes boundary. *Quaternary Geochronology*, *39*, 1–23. https://doi.org/10.1016/j.quageo.2017.01.002

Mazaud, A., Channell, J., & Stoner, J. (2012). Relative paleointensity and environmental magnetism since 1.2 Ma at IODP site U1305 (Eirik drift, NW Atlantic). *Earth and Planetary Science Letters*, *357*, 137–144. https://doi.org/10.1016/j.epsl.2012.09.037

Mazaud, A., Channell, J., & Stoner, J. (2015). The paleomagnetic record at IODP Site U1307 back to 2.2 Ma (Eirik Drift, off south Greenland). *Earth and Planetary Science Letters*, *429*, 82–89. https://doi.org/10.1016/j.epsl.2015.07.059

McDowell, F. W. (1983). K-Ar dating: Incomplete extraction of radiogenic argon from alkali feldspar. *Chemical Geology*, *41*, 119–126. https://doi.org/10.1016/s0009-2541(83)80012-6

Meynadier, L., Valet, J.-P., Bassinot, F. C., Shackleton, N. J., & Guyodo, Y. (1994). Asymmetrical saw-tooth pattern of the geomagnetic field intensity from equatorial sediments in the Pacific and Indian Oceans. *Earth and Planetary Science Letters*, *126*(1–3), 109–127. https://doi.org/10.1016/0012-821x(94)90245-3

Meynadier, L., Valet, J.-P., & Shackleton, N. J. (1995). Relative geomagnetic intensity during the last 4 My from the equatorial Pacific. In N. G. Pisias, L. A. Mayer, T. R. Janecek, A. Palmer-Julson, & T. H. van Andel (Eds.), *Proceedings of the Ocean Drilling Program, Scientific Result* (Vol. 138, pp. 779–795). ODP.

Michalk, D. M., Biggin, A. J., Knudsen, M. F., Böhnel, H. N., Nowaczyk, N. R., Ownby, S., & López-Martínez, M. (2010). Application of the multispecimen palaeointensity method to Pleistocene lava flows from the Trans-Mexican Volcanic Belt. *Physics of the Earth and Planetary Interiors*, *179*(3–4), 139–156. https://doi.org/10.1016/j.pepi.2010.01.005

Min, K., Mundil, R., Renne, P. R., & Ludwig, K. R. (2000). A test for systematic errors in $^{40}Ar/^{39}Ar$ geochronology through comparison with U/Pb analysis of a 1.1-Ga rhyolite. *Geochimica et Cosmochimica Acta*, *64*(1), 73–98. https://doi.org/10.1016/s0016-7037(99)00204-5

Mochizuki, N., Oda, H., Ishizuka, O., Yamazaki, T., & Tsunakawa, H. (2011). Paleointensity variation across the Matuyama-Brunhes polarity transition: Observations from lavas at Punaruu valley, Tahiti. *Journal of Geophysical Research*, *116*(B6), B06103. https://doi.org/10.1029/2010jb008093

Néel, L. (1955). Some theoretical aspects of rock-magnetism. *Advances in Physics*, *4*(14), 191–243. https://doi.org/10.1080/00018735500101204

Nelson, S. A., & González-Caver, E. (1992). Geology and K-Ar dating of the Tuxtla volcanic field, Veracruz, Mexico. *Bulletin of Volcanology*, *55*(1), 85–96. https://doi.org/10.1007/bf00301122

Nowaczyk, N. R., Haltia, E., Ulbricht, D., Wennrich, V., Sauerbrey, M., Rosén, P., et al. (2013). Chronology of Lake El'gygytgyn sediments–a combined magnetostratigraphic, palaeoclimatic and orbital tuning study based on multi-parameter analyses. *Climate of the Past*, *9*(6), 2413–2432. https://doi.org/10.5194/cp-9-2413-2013

Oda, H., Nakazato, H., Nanayama, F., & Harigane, Y. (2022). Matuyama–Brunhes geomagnetic reversal record and associated key tephra layers in Boso Peninsula: Extraction of primary magnetization of geomagnetic fields from mixed magnetic minerals of depositional, diagenesis, and weathering processes. *Earth Planets and Space*, *74*(1), 1–29. https://doi.org/10.1186/s40623-022-01626-1

Oda, H., Shibuya, H., & Hsu, V. (2000). Palaeomagnetic records of the Brunhes/Matuyama polarity transition from ODP Leg 124 (Celebes and Sulu seas). *Geophysical Journal International*, *142*(2), 319–338. https://doi.org/10.1046/j.1365-246x.2000.00130.x

Ogg, J. (2020). Geomagnetic polarity time scale. In *Geologic time scale 2020* (pp. 159–192). Elsevier.

Ownby, S., Granados, H. D., Lange, R. A., & Hall, C. M. (2007). Volcán Tancítaro, Michoacán, Mexico, $^{40}Ar/^{39}Ar$ constraints on its history of sector collapse. *Journal of Volcanology and Geothermal Research*, *161*(1–2), 1–14. https://doi.org/10.1016/j.jvolgeores.2006.10.009

Panovska, S., & Constable, C. (2017). An activity index for geomagnetic paleosecular variation, excursions, and reversals. *Geochemistry, Geophysics, Geosystems*, *18*(4), 1366–1375. https://doi.org/10.1002/2016gc006668

Panovska, S., Finlay, C. C., Donadini, F., & Hirt, A. M. (2012). Spline analysis of Holocene sediment magnetic records: Uncertainty estimates for field modeling. *Journal of Geophysical Research*, *117*(B2), B02101. https://doi.org/10.1029/2011jb008813

Panovska, S., Korte, M., & Constable, C. G. (2019). One hundred thousand years of geomagnetic field evolution. *Reviews of Geophysics*, *57*(4), 1289–1337. https://doi.org/10.1029/2019rg000656

Panovska, S., Korte, M., Liu, J., & Nowaczyk, N. (2021). Global evolution and dynamics of the geomagnetic field in the 15–70 Kyr period based on selected paleomagnetic sediment records. *Journal of Geophysical Research: Solid Earth*, *126*(12), e2021JB022681. https://doi.org/10.1029/2021jb022681

Prévot, M., & Camps, P. (1993). Absence of preferred longitude sectors for poles from volcanic records of geomagnetic reversals. *Nature*, *366*(6450), 53–57. https://doi.org/10.1038/366053a0

Quidelleur, X., Carlut, J., Gillot, P.-Y., & Soler, V. (2002). Evolution of the geomagnetic field prior to the Matuyama—Brunhes transition: Radiometric dating of a 820 ka excursion at La Palma. *Geophysical Journal International*, *151*(2), F6–F10. https://doi.org/10.1046/j.1365-246x.2002.01841.x

Quidelleur, X., Carlut, J., Soler, V., Valet, J.-P., & Gillot, P.-Y. (2003). The age and duration of the Matuyama–Brunhes transition from new K–Ar data from La Palma (Canary Islands) and revisited $^{40}Ar/^{39}Ar$ ages. *Earth and Planetary Science Letters*, *208*(3–4), 149–163. https://doi.org/10.1016/s0012-821x(03)00053-0

Quidelleur, X., Gillot, P.-Y., Soler, V., & Lefèvre, J.-C. (2001). K/Ar dating extended into the last millennium: Application to the youngest effusive episode of the Teide volcano (Spain). *Geophysical Research Letters*, *28*(16), 3067–3070. https://doi.org/10.1029/2000gl012821

Quidelleur, X., & Valet, J.-P. (1996). Geomagnetic changes across the last reversal recorded in lava flows from La Palma, Canary Islands. *Journal of Geophysical Research*, *101*(B6), 13755–13773. https://doi.org/10.1029/95jb03740

Raisbeck, G., Yiou, F., Cattani, O., & Jouzel, J. (2006). ^{10}Be evidence for the Matuyama–Brunhes geomagnetic reversal in the EPICA Dome C ice core. *Nature*, *444*(7115), 82–84. https://doi.org/10.1038/nature05266

Renne, P. R., Swisher, C. C., Deino, A. L., Karner, D. B., Owens, T. L., & DePaolo, D. J. (1998). Intercalibration of standards, absolute ages and uncertainties in ^{40}Ar/^{39}Ar dating. *Chemical Geology*, *145*(1–2), 117–152. https://doi.org/10.1016/s0009-2541(97)00159-9

Ricci, J., Carlut, J., Marques, F. O., Hildenbrand, A., & Valet, J.-P. (2020). Volcanic record of the last geomagnetic reversal in a lava flow sequence from the Azores. *Frontiers of Earth Science*, *8*, 165. https://doi.org/10.3389/feart.2020.00165

Ricci, J., Carlut, J., & Valet, J.-P. (2018). Paleosecular variation recorded by Quaternary lava flows from Guadeloupe Island. *Scientific Reports*, *8*(1), 1–14. https://doi.org/10.1038/s41598-018-28384-z

Ricci, J., Quidelleur, X., Pallares, C., & Lahitte, P. (2017). High-resolution K-Ar dating of a complex magmatic system: The example of Basse-Terre Island (French West Indies). *Journal of Volcanology and Geothermal Research*, *345*, 142–160. https://doi.org/10.1016/j.jvolgeores.2017.07.013

Roberts, A. P. (2006). High-resolution magnetic analysis of sediment cores: Strengths, limitations and strategies for maximizing the value of long-core magnetic data. *Physics of the Earth and Planetary Interiors*, *156*(3–4), 162–178. https://doi.org/10.1016/j.pepi.2005.03.021

Roberts, A. P., & Winklhofer, M. (2004). Why are geomagnetic excursions not always recorded in sediments? Constraints from post-depositional remanent magnetization lock-in modelling. *Earth and Planetary Science Letters*, *227*(3–4), 345–359. https://doi.org/10.1016/j.epsl.2004.07.040

Sagnotti, L., Budillon, F., Dinarès-Turell, J., Iorio, M., & Macrì, P. (2005). Evidence for a variable paleomagnetic lock-in depth in the Holocene sequence from the Salerno Gulf (Italy): Implications for "high-resolution" paleomagnetic dating. *Geochemistry, Geophysics, Geosystems*, *6*(11), Q11013. https://doi.org/10.1029/2005gc001043

Sagnotti, L., Giaccio, B., Liddicoat, J. C., Caricchi, C., Nomade, S., & Renne, P. R. (2019). On the reliability of the Matuyama–Brunhes record in the Sulmona basin—Comment to 'A reappraisal of the proposed rapid Matuyama–Brunhes geomagnetic reversal in the Sulmona basin, Italy'by Evans and Muxworthy (2018). *Geophysical Journal International*, *216*(1), 296–301. https://doi.org/10.1093/gji/ggy427

Sagnotti, L., Giaccio, B., Liddicoat, J. C., Nomade, S., Renne, P. R., Scardia, G., & Sprain, C. J. (2016). How fast was the Matuyama–Brunhes geomagnetic reversal? A new subcentennial record from the Sulmona basin, central Italy. *Geophysical Journal International*, *204*(2), 798–812. https://doi.org/10.1093/gji/ggv486

Sagnotti, L., Scardia, G., Giaccio, B., Liddicoat, J. C., Nomade, S., Renne, P. R., & Sprain, C. J. (2014). Extremely rapid directional change during Matuyama-Brunhes geomagnetic polarity reversal. *Geophysical Journal International*, *199*(2), 1110–1124. https://doi.org/10.1093/gji/ggu287

Sakuramoto, Y., Yamazaki, T., Kimoto, K., Miyairi, Y., Kuroda, J., Yokoyama, Y., & Matsuzaki, H. (2017). A geomagnetic paleointensity record of 0.6 to 3.2 Ma from sediments in the Western Equatorial Pacific and remanent magnetization lock-in depth. *Journal of Geophysical Research: Solid Earth*, *122*(10), 7525–7543. https://doi.org/10.1002/2017jb014450

Samper, A., Quidelleur, X., Lahitte, P., & Mollex, D. (2007). Timing of effusive volcanism and collapse events within an oceanic arc island: Basse-Terre, Guadeloupe archipelago (Lesser Antilles Arc). *Earth and Planetary Science Letters*, *258*(1–2), 175–191. https://doi.org/10.1016/j.epsl.2007.03.030

Sarna-Wojcicki, A. M., Pringle, M. S., & Wijbrans, J. (2000). New ^{40}Ar/^{39}Ar age of the Bishop Tuff from multiple sites and sediment rate calibration for the Matuyama-Brunhes boundary. *Journal of Geophysical Research*, *105*(B9), 21431–21443. https://doi.org/10.1029/2000jb900091

Sato, T., Kikuchi, H., Nakashizuka, M., & Okada, M. (1998). Quaternary geomagnetic field intensity: Constant periodicity or variable period? *Geophysical Research Letters*, *25*(12), 2221–2224. https://doi.org/10.1029/98gl01621

Sato, T., & Kobayashi, K. (1989). Long-period secular variations of the Earth's magnetic field revealed by Pacific deep-sea sediment cores. *Journal of Geomagnetism and Geoelectricity*, *41*(1), 147–159. https://doi.org/10.5636/jgg.41.147

Schaen, A., Jicha, B., Hodges, K., Vermeesch, P., Stelten, M., Mercer, C., et al. (2020). Interpreting and reporting ^{40}Ar/^{39}Ar geochronologic data. *GSA Bulletin*, *133*(3–4), 461–487. https://doi.org/10.1130/b35560.1

Schnepp, E., & Hradetzky, H. (1994). Combined paleointensity and ^{40}Ar/^{39}Ar age spectrum data from volcanic rocks of the West Eifel field (Germany): Evidence for an early Brunhes geomagnetic excursion. *Journal of Geophysical Research*, *99*(B5), 9061–9076. https://doi.org/10.1029/93jb03365

Shackleton, N., Berger, A., & Peltier, W. (1990). An alternative astronomical calibration of the lower Pleistocene timescale based on ODP Site 677. *Earth and Environmental Science Transactions of the Royal Society of Edinburgh*, *81*(4), 251–261. https://doi.org/10.1017/s0263593300020782

Shackleton, N., Crowhurst, S., Hagelberg, T., Pisias, N., & Schneider, D. (1995). A new Late Neogene time scale: Application to Leg 138 sites. *Proceedings of the Ocean Drilling Program, Scientific Result*, *138*, 73–101.

Shao, J.-C., Fuller, M., Tanimoto, T., Dunn, J., & Stone, D. (1999). Spherical harmonic analyses of paleomagnetic data: The time-averaged geomagnetic field for the past 5 Myr and the Brunhes-Matuyama reversal. *Journal of Geophysical Research*, *104*(B3), 5015–5030. https://doi.org/10.1029/98jb01354

Shaw, J. (1974). A new method of determining the magnitude of the palaeomagnetic field: Application to five historic lavas and five archaeological samples. *Geophysical Journal International*, *39*(1), 133–141. https://doi.org/10.1111/j.1365-246x.1974.tb05443.x

Shin, J. Y., Yu, Y., & Kim, W. (2019). Wavelet-based verification of a relative paleointensity record from the North Pacific. *Earth Planets and Space*, *71*(1), 1–14. https://doi.org/10.1186/s40623-019-1067-x

Singer, B. (2014). A Quaternary geomagnetic instability time scale. *Quaternary Geochronology*, *21*, 29–52. https://doi.org/10.1016/j.quageo.2013.10.003

Singer, B., Hoffman, K. A., Coe, R. S., Brown, L. L., Jicha, B. R., Pringle, M. S., & Chauvin, A. (2005). Structural and temporal requirements for geomagnetic field reversal deduced from lava flows. *Nature*, *434*(7033), 633–636. https://doi.org/10.1038/nature03431

Singer, B., Hoffman, K. A., Schnepp, E., & Guillou, H. (2008). Multiple Brunhes Chron excursions recorded in the West Eifel (Germany) volcanics: Support for long-held mantle control over the non-axial dipole field. *Physics of the Earth and Planetary Interiors*, *169*(1–4), 28–40. https://doi.org/10.1016/j.pepi.2008.05.001

Singer, B., Jicha, B. R., Mochizuki, N., & Coe, R. S. (2019). Synchronizing volcanic, sedimentary, and ice core records of Earth's last magnetic polarity reversal. *Science Advances*, *5*(8), eaaw4621. https://doi.org/10.1126/sciadv.aaw4621

Singer, B., Relle, M., Hoffman, K., Battle, A., Laj, C., Guillou, H., & Carracedo, J. (2002). Ar/Ar ages from transitionally magnetized lavas on La Palma, Canary Islands, and the geomagnetic instability timescale. *Journal of Geophysical Research*, *107*(B11), EPM–7–EPM7-20. https://doi.org/10.1029/2001jb001613

Suganuma, Y., Okada, M., Horie, K., Kaiden, H., Takehara, M., Senda, R., et al. (2015). Age of Matuyama-Brunhes boundary constrained by U-Pb zircon dating of a widespread tephra. *Geology*, *43*(6), 491–494. https://doi.org/10.1130/g36625.1

Tauxe, L. (2010). *Essentials of paleomagnetism*. University of California Press.

Tauxe, L., Gans, P., & Mankinen, E. A. (2004). Paleomagnetism and $^{40}Ar/^{39}Ar$ ages from volcanics extruded during the Matuyama and Brunhes Chrons near McMurdo sound, Antarctica. *Geochemistry, Geophysics, Geosystems*, *5*(6), Q06H12. https://doi.org/10.1029/2003gc000656

Tauxe, L., & Staudigel, H. (2004). Strength of the geomagnetic field in the Cretaceous normal superchron: New data from submarine basaltic glass of the Troodos Ophiolite. *Geochemistry, Geophysics, Geosystems*, *5*(2), Q02H06. https://doi.org/10.1029/2003gc000635

Tauxe, L., Valet, J.-P., & Bloemendal, J. (1989). The magnetostratigraphy of Leg 108 APC cores. In *Proceeding of the ocean drilling program* (pp. 865–880).

Tauxe, L., & Yamazaki, T. (2007). Paleointensities, in geomagnetism. *Treatise on Geophysics*, *5*, 509–563.

Tauxe, L., & Yamazaki, T. (2015). Paleointensities. In G. Schubert (Ed.), *Treatise on geophysics*, (2nd ed., pp. 461–509). Elsevier. https://doi.org/10.1016/B978-0-444-53802-4.00107-X

Thellier, E., & Thellier, O. (1959). Sur l'intensité du champ magnétique terrestre dans le passé historique et géologique. *Annales Geophysicae*, *15*, 285–376.

Tsunakawa, H., & Shaw, J. (1994). The Shaw method of palaeointensity determinations and its application to recent volcanic rocks. *Geophysical Journal International*, *118*(3), 781–787. https://doi.org/10.1111/j.1365-246x.1994.tb03999.x

Ucar, H., Kletetschka, G., & Kadlec, J. (2021). Evidence of the Matuyama-Brunhes transition in cave sediment in Central Europe. *Quaternary International*, *604*, 16–27. https://doi.org/10.1016/j.quaint.2021.07.005

Valet, J.-P., Bassinot, F., Bouilloux, A., Bourlès, D., Nomade, S., Guillou, V., et al. (2014). Geomagnetic, cosmogenic and climatic changes across the last geomagnetic reversal from equatorial Indian Ocean sediments. *Earth and Planetary Science Letters*, *397*, 67–79. https://doi.org/10.1016/j.epsl.2014.03.053

Valet, J.-P., Bassinot, F., Simon, Q., Savranskaia, T., Thouveny, N., Bourlés, D. L., & Villedieu, A. (2019). Constraining the age of the last geomagnetic reversal from geochemical and magnetic analyses of Atlantic, Indian, and Pacific Ocean sediments. *Earth and Planetary Science Letters*, *506*, 323–331. https://doi.org/10.1016/j.epsl.2018.11.012

Valet, J.-P., Brassart, J., Quidelleur, X., Soler, V., Gillot, P.-Y., & Hongre, L. (1999). Paleointensity variations across the last geomagnetic reversal at La Palma, Canary Islands, Spain. *Journal of Geophysical Research*, *104*(B4), 7577–7598. https://doi.org/10.1029/1998jb900099

Valet, J.-P., & Fournier, A. (2016). Deciphering records of geomagnetic reversals. *Reviews of Geophysics*, *54*(2), 410–446. https://doi.org/10.1002/2015rg000506

Valet, J.-P., Fournier, A., Courtillot, V., & Herrero-Bervera, E. (2012). Dynamical similarity of geomagnetic field reversals. *Nature*, *490*(7418), 89–93. https://doi.org/10.1038/nature11491

Valet, J.-P., & Meynadier, L. (1993). Geomagnetic field intensity and reversals during the past four million years. *Nature*, *366*(6452), 234–238. https://doi.org/10.1038/366234a0

Valet, J.-P., Meynadier, L., Bassinot, F. C., & Garnier, F. (1994). Relative paleointensity across the last geomagnetic reversal from sediments of the Atlantic, Indian and Pacific Oceans. *Geophysical Research Letters*, *21*(6), 485–488. https://doi.org/10.1029/93gl02815

Valet, J.-P., Meynadier, L., & Guyodo, Y. (2005). Geomagnetic dipole strength and reversal rate over the past two million years. *Nature*, *435*(7043), 802–805. https://doi.org/10.1038/nature03674

Valet, J.-P., Meynadier, L., Simon, Q., & Thouveny, N. (2016). When and why sediments fail to record the geomagnetic field during polarity reversals. *Earth and Planetary Science Letters*, *453*, 96–107. https://doi.org/10.1016/j.epsl.2016.07.055

Valet, J.-P., Tauxe, L., & Clark, D. R. (1988). The Matuyama-Brunhes transition recorded from Lake Tecopa sediments (California). *Earth and Planetary Science Letters*, *87*(4), 463–472. https://doi.org/10.1016/0012-821x(88)90009-x

Valet, J.-P., Tauxe, L., & Clement, B. (1989). Equatorial and mid-latitude records of the last geomagnetic reversal from the Atlantic Ocean. *Earth and Planetary Science Letters*, *94*(3–4), 371–384. https://doi.org/10.1016/0012-821x(89)90154-4

Valet, J.-P., Thevarasan, A., Bassinot, F., Savranskaia, T., & Haddam, N. (2020). Two records of relative paleointensity for the past 4 Myr. *Frontiers of Earth Science*, *8*, 148. https://doi.org/10.3389/feart.2020.00148

Van Zijl, J., Graham, K., & Hales, A. (1962). The palaeomagnetism of the Stormberg Lavas, II. The behaviour of the magnetic field during a reversal. *Geophysical Journal of the Royal Astronomical Society*, *7*(2), 169–182. https://doi.org/10.1111/j.1365-246x.1962.tb00366.x

Wang, X., Løvlie, R., Chen, Y., Yang, Z., Pei, J., & Tang, L. (2014). The Matuyama–Brunhes polarity reversal in four Chinese loess records: High-fidelity recording of geomagnetic field behavior or a less than reliable chronostratigraphic marker? *Quaternary Science Reviews*, *101*, 61–76. https://doi.org/10.1016/j.quascirev.2014.07.005

Webb, A., & McDougall, I. (1967). A comparison of mineral and whole rock potassium-argon ages of Tertiary volcanics from central Queensland, Australia. *Earth and Planetary Science Letters*, *3*, 41–47. https://doi.org/10.1016/0012-821x(67)90009-x

Wicht, J. (2005). Palaeomagnetic interpretation of dynamo simulations. *Geophysical Journal International*, *162*(2), 371–380. https://doi.org/10.1111/j.1365-246x.2005.02665.x

Wicht, J., Stellmach, S., & Harder, H. (2009). Numerical models of the geodynamo: From fundamental Cartesian models to 3D simulations of field reversals. In *Geomagnetic field variations* (pp. 107–158). Springer.

Wilch, T. I. (1991). Surficial geology and geochronology of middle Taylor Valley, Antarctica. M.S. thesis, University of Maine.

Wu, Y., Zhu, Z., Qiu, S., Han, Y., Cai, J., & Rao, Z. (2016). Magnetic stratigraphy constraints on the Matuyama–Brunhes boundary recorded in a loess section at the southern margin of Chinese Loess Plateau. *Geophysical Journal International*, *204*(2), 1072–1085. https://doi.org/10.1093/gji/ggv502

Xuan, C., Channell, J., & Hodell, D. A. (2016). Quaternary magnetic and oxygen isotope stratigraphy in diatom-rich sediments of the southern Gardar Drift (IODP Site U1304, North Atlantic). *Quaternary Science Reviews*, *142*, 74–89. https://doi.org/10.1016/j.quascirev.2016.04.010

Yamazaki, T. (1999). Relative paleointensity of the geomagnetic field during Brunhes Chron recorded in North Pacific deep-sea sediment cores: Orbital influence? *Earth and Planetary Science Letters*, *169*(1–2), 23–35. https://doi.org/10.1016/s0012-821x(99)00064-3

Yamazaki, T., Ioka, N., & Eguchi, N. (1995). Relative paleointensity of the geomagnetic field during the Brunhes Chron. *Earth and Planetary Science Letters*, *136*(3–4), 525–540. https://doi.org/10.1016/0012-821x(95)00189-j

Yamazaki, T., & Kanamatsu, T. (2007). A relative paleointensity record of the geomagnetic field since 1.6 Ma from the North Pacific. *Earth Planets and Space*, *59*(7), 785–794. https://doi.org/10.1186/bf03352741

Yamazaki, T., & Oda, H. (2005). A geomagnetic paleointensity stack between 0.8 and 3.0 Ma from equatorial Pacific sediment cores. *Geochemistry, Geophysics, Geosystems*, *6*(11), Q11H20. https://doi.org/10.1029/2005gc001001

Yamazaki, T., & Yamamoto, Y. (2018). Relative paleointensity and inclination anomaly over the last 8 Myr obtained from the Integrated Ocean Drilling Program Site U1335 sediments in the eastern equatorial Pacific. *Journal of Geophysical Research: Solid Earth*, *123*(9), 7305–7320. https://doi.org/10.1029/2018jb016209

Zhou, W., Warren Beck, J., Kong, X., An, Z., Qiang, X., Wu, Z., et al. (2014). Timing of the Brunhes-Matuyama magnetic polarity reversal in Chinese loess using ^{10}Be. *Geology*, *42*(6), 467–470. https://doi.org/10.1130/g35443.1

Ziegler, L., Constable, C., Johnson, C., & Tauxe, L. (2011). PADM2M: A penalized maximum likelihood model of the 0–2 Ma palaeomagnetic axial dipole moment. *Geophysical Journal International*, *184*(3), 1069–1089. https://doi.org/10.1111/j.1365-246x.2010.04905.x